International Journal of Heat and Mass Transfer 229 (2024) 125706

Contents lists available at ScienceDirect

International Journal of Heat and Mass Transfer

journal homepage: www.elsevier.com/locate/hmt

Amplitude modulation of turbulence intensities and fluxes in urban convective boundary layers

Kangcheng Zhou [a,b,c], Chun-Ho Liu [c], Di Mei [c], Buchen Wu [a,b,d,*], Minping Wan [a,b,*]

[a] Guangdong Provincial Key Laboratory of Turbulence Research and Applications, Department of Mechanics and Aerospace Engineering, Southern University of Science and Technology, Shenzhen, 518055, PR China

[b] Guangdong-Hong Kong-Macao Joint Laboratory for Data-Driven Fluid Mechanics and Engineering Applications, Southern University of Science and Technology, Shenzhen, 518055, PR China

[c] Department of Mechanical Engineering, The University of Hong Kong, 7/F, Haking Wong Building, Pokfulam Road, Hong Kong Special Administrative Region of China

[d] Department of Mechanical and Aerospace Engineering, The Hong Kong University of Science and Technology, Clear Water Bay, Hong Kong Special Administrative Region of China

ARTICLE INFO

Keywords:
Urban turbulence
Amplitude modulation
Unstable stratification
Coherent structures
Turbulent convection

ABSTRACT

Despite extensive research on the effect of atmospheric stability, the influence of convective rolls and thermal plumes in convective boundary layer (CBL) on urban winds and turbulence remains merely understood. Using amplitude modulation (AM), we examine the multi-scale interaction among turbulence intensities, fluxes, and large-scale CBL structures in unstable urban boundary layers (UBLs). Nine sets of large-eddy simulation (LES) are conducted, contrasting the CBL behavior over idealized urban morphology from neutral to free convection. This study, comparing the stability-dependent AM coefficient, reveals a tight modulation of small-scale turbulence and fluxes at urban canopy layer (UCL) by different types of characteristic CBL structures. Wavelet analysis corroborates their interactions in the time-frequency domain. Moreover, the correlation between the AM and the coherent CBL structures in the mixed layers is unveiled. Additionally, building-induced secondary flow structures are observed to dominate the modulation of small-scale turbulence residing within. UCL building-scale turbulence exhibits a higher susceptibility to modulation compared with intermediate scales. Notably, strong convection can invert the phase relationship between large scales and UCL turbulence. These results signify the crucialness of considering CBL coherent structures in the development of land-surface-parameterization schemes as well as the cautious implementation of predictive models in urban CBLs.

1. Introduction

Flourishing city expansion was evidenced by the surge of urban population from 751 million in 1950 to 4.2 billion in 2018. Currently, 55% of the global population resides in urban areas that is anticipated to escalate to 68% by 2050 [1]. Urban inhabitants are particularly vulnerable to weather-related health hazards, such as heatstroke during heatwaves or respiratory illnesses aggravated by poor air quality [2]. Numerical weather prediction (NWP) models over built areas facilitate the forecasting of weather conditions therein, enabling government or authorities to issue timely warnings and preventive measures.

Land-surface parameterization plays a key role in NWP because it models those under-resolved physical processes within urban canopy layers (UCLs). Comparing the findings between the Weather Research and Forecasting (WRF) model and the Joint Urban 2003 field campaign in Oklahoma City unveiled the disparity in which the turbulence- and thermal-related statistics, such as turbulence kinetic energy (TKE), Obukhov length L, and heat flux σ, were particularly noticeable [3]. These discrepancies are predominantly attributed to the current (over-) simplified UCL models. For instance, only local factors, such as the street-canyon aspect ratio and mean wind direction/speed, are considered [4].

Nonlocal factors, such as spatially heterogeneous urban roughness and heating sources, have been identified as the key contributors to the transport of TKE and heat [5,6]. A recent field measurement explored the budgets of TKE and heat within urban RSLs [7] in which the residual terms of local budget balance accounted for substantial proportions (40% to 50% in potential temperature budget). These findings signify the potential roles of nonlocal factors in the dynamics in urban canopies, which, however, are not accounted for in the majority

* Corresponding authors.
E-mail addresses: buchenwu@ust.hk (B. Wu), wanmp@sustech.edu.cn (M. Wan).

https://doi.org/10.1016/j.ijheatmasstransfer.2024.125706
Received 27 February 2024; Received in revised form 28 April 2024; Accepted 9 May 2024
Available online 23 May 2024

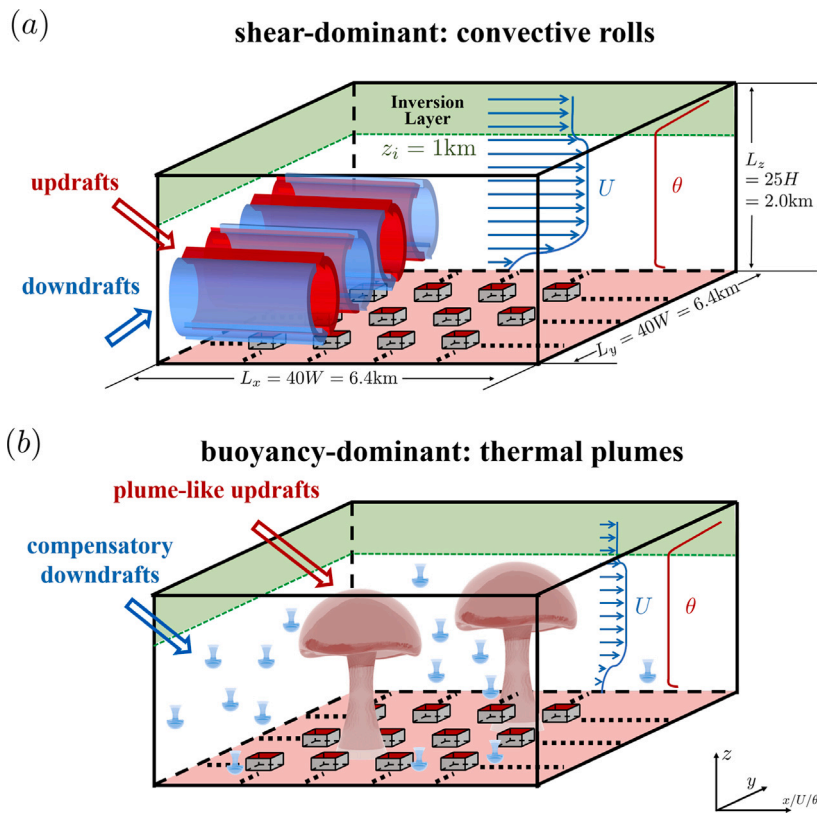

Fig. 1. Schematic of the computational domain and key physical phenomena: typical profiles of streamwise velocity u and potential temperature θ, inversion layer, and CBL structures under (a) shear- and (b) buoyancy-dominant states. Building façades are depicted in gray. Rooftops and ground surfaces are highlighted in red and pink, respectively, on which heat is imposed.

of single-layer or multi-layer UCL models [8,9]. Large-scale motions (LSMs; whose characteristic length scale is longer than the inversion height z_i) in the form of coherent structures exist that are crucial to atmospheric transport [10]. In view of the scales, they are identified as nonlocal contributors to UCL dynamics. However, LSMs are often overlooked in the land-surface parameterizations in the modeling of atmospheric boundary layers (ABLs).

In view of the aforementioned (modeling) knowledge gap, this study is conceived to examine the coherent structures in the ABLs over explicitly resolved, hypothetical urban morphology in a range of unstable stratification using the large-eddy simulation (LES). In particular, we contrast the interaction among the flows and thermals by amplitude modulation (AM) as well as motion-scale partitioning.

Isothermal, turbulent flows are characterized by coherent structures. For instance, the elongated, very large-scale motions (VLSMs; longer than $10z_i$) dominate the organized structures in wall-bounded turbulence [11,12]. Their concept was initiated by observing two peaks in the premultiplied power spectral density (PSD) of streamwise velocity fluctuations [13]. The peaked PSD at a lower wavenumber signified that the flow structures are substantially larger than the known LSMs. The origin of VLSMs is debatable. It might arise from either the coalescence of hairpin vortices (bottom-up mechanism) [14] or outer-layer fluctuations (top-down mechanism) [15]. Subsequent studies have emphasized the pivotal roles of VLSMs which contribute as much as 50% to 60% to the TKE or the momentum flux [16]. Moreover, these coherent structures would entrain into the viscous sublayers [17], interacting with the even smaller, near-wall turbulence [18].

The shear and buoyancy mechanism in convective boundary layers (CBLs) collectively influence the coherent structures, which, however, deviate from those of the classical similarity theory [10]. In the shear-dominant regime, CBL flow structures are prevalently quasi-2D convective rolls (Fig. 1). In brief, near-wall, low-momentum fluids elevate the temperature (locally). The buoyancy-driven updrafts then induce the coherent convective rolls [19]. The onset of convective rolls has been demonstrated by higher-resolution LES computations [20], linear stability theory [21], as well as resolvent analysis [22].

In buoyancy-dominant regime, on the other hand, near-wall eddies develop into cellular plumes (Fig. 1) which are characterized by intense, spur-like updrafts alongside weak, broad downdrafts [23]. The transition from roll- to cell-type structures occurs around the stability parameter ζ ($= -z_i/L$; [24,25]) in the range of $15 \leq \zeta \leq 20$ [26]. The aforementioned CBL flow structures are modified in the presence of surface-mounted roughness elements [27,28], which, however, have been merely studied.

Interaction between large-scale coherent structures and near-wall turbulence is crucial in wall-bounded flows. The AM coefficient, which is derived from Hilbert transform and low-pass filtering, was introduced to quantify the multi-scale dynamics modulation [18]. It was found that small-scale turbulence is intensified and diminished, respectively, during accelerating and decelerating VLSMs in the near-wall region. Another study later confirmed that all three velocity components are modulated simultaneously by VLSMs [29]. Furthermore, there exists a cross term in the scale-decomposed skewness of streamwise velocity that has been identified as an effective diagnosis for AM examination [30]. A theoretical derivation based on triadic scale interactions was established to elucidate the relationship between AM coefficient and velocity skewness [31].

A more profound comprehension of AM facilitates the formulation of predictive models that are capable of estimating near-wall, small-scale turbulence based solely on outer-layer flows [12]. Moreover, it fostered the framework for the LES wall model development [32].

Recent research has increasingly focused on the AM phenomena in urban flows due to their practical importance. Pioneering studies have employed high-fidelity computer models to explore the AM over ribs in

crossflows [33] and staggered cubes [34]. In the roughness sublayers (RSLs) over explicitly resolved roughness elements, the AM and coherent structures are tightly coupled in which modulation is prominent at the front edges in high-momentum regions but is reduced in low-momentum regions [35]. Lately, studies have extended from idealized to real urban morphology numerically [36] and experimentally [37] whose findings concurred with those from idealized urban morphology. Moreover, the practical potential of predictive models in urban flows was demonstrated [38].

Apart from isothermal flows, a handful of studies have investigated the influence of ABL thermal stratification on AM. Aircraft data detected that AM is largely attributed to the large-scale vertical flows in convective rolls [39]. Recently, the buoyancy effect on LSMs in CBLs, particularly in modulating near-wall processes, was evaluated by LESs [24]. It was observed that buoyancy-induced AM varies across atmospheric stability. The modulation by large-scale streamwise flows remains significant in weak convection. It is lessened in more unstable conditions in which the prevailing flows are gradually switching from streamwise to vertical dominance. Using the field measurements over homogeneous grassland, a linear relation was established to express AM in terms of atmospheric stability [40]. Despite the aforementioned studies, investigations into the effect of atmospheric stability on AM remain scanty compared with those in neutral conditions.

As reviewed above, the majority of studies have emphasized the AM in isothermal turbulent boundary layers (TBLs) and canonical CBLs. Although some studies have investigated the influence of unstable ABL on the mean and turbulent flows in proximity to buildings [41–44], the impact of large-scale CBL structures on UCL turbulence has not been examined. To address the aforementioned knowledge gap, LES is employed to analyze AM phenomena in this paper. Our investigation spans from shear (neutral) to buoyancy (unstable) dominant ABLs, encompassing both convective rolls and thermal plumes in CBLs. To the best knowledge of the authors, this study is the first attempt to investigate the AM in urban CBLs.

This section reviews the relevant literature and states the key scientific contributions and the core research questions. The LES setting and the analytical approaches are described in Section 2. Section 3 outlines the approach to the data analyses. In Section 4, the findings, focusing on the impact of buoyancy on the AM in urban CBLs, are presented, The phase relationship and its spatial variability are also discussed. Finally, Section 5 draws the conclusions as well as highlights the practical implications harvested from this paper.

2. Mathematical model

2.1. Governing equations

This study employs the LES of incompressible flows with heat transfer based on the Boussinesq approximation. The governing equations for the conservation of mass, momentum, and potential temperature in resolved scales (denoted by overbar $\overline{\xi}$ for a variable ξ) are

$$\frac{\partial \overline{u}_i}{\partial x_i} = 0\,, \tag{1}$$

$$\frac{\partial \overline{u}_i}{\partial t} + \frac{\partial\left(\overline{u}_i\overline{u}_j\right)}{\partial x_j} = -\left(\frac{\partial \overline{\Pi}}{\partial x_i} + \frac{\partial P}{\partial x_i}\right) + \nu\frac{\partial^2 \overline{u}_i}{\partial x_j \partial x_j} + \frac{\overline{\theta}-\Theta_0}{\Theta_0}g_i - \frac{\partial \tau_{ij}^d}{\partial x_j}\,, \tag{2}$$

and

$$\frac{\partial \overline{\theta}}{\partial t} + \frac{\partial\left(\overline{u}_j\overline{\theta}\right)}{\partial x_j} = \frac{\nu}{Pr}\frac{\partial^2 \overline{\theta}}{\partial x_j \partial x_j} - \frac{\partial \sigma_j}{\partial x_j}\,, \tag{3}$$

respectively. Here, x_i (= x, y, z) is the Cartesian coordinate, u_i (= u, v, w) the velocity vector; θ the potential temperature; Θ_0 (= 300 K) the reference potential temperature; ν (= 1×10^{-5} m^2 s^{-1}) the kinematic viscosity; Pr (= 0.7) the Prandtl number; g_i (= 0, 0, −9.81 m s^{-2}) the gravitational acceleration vector; p the kinematic pressure; Π (= $p + \tau_{kk}/3$) the modified kinematic pressure; τ_{ij} (= $\overline{u_iu_j} - \overline{u}_i\overline{u}_j$) the subgrid-scale (SGS) momentum flux; τ_{kk} the trace of τ_{ij}; σ_j (= $\overline{u_j\theta} - \overline{u}_j\overline{\theta}$) the SGS potential temperature flux; and $\partial P/\partial x_i$ the mean kinematic pressure gradient prescribed at the background. To mitigate the complexity introduced by wind veering, which varies with height and atmospheric stability [26] together with complicates the wind incident angle across different cases, the Coriolis term is excluded from Eq. (2). This simplification facilitates the simulations to accurately capture the essential CBL characteristics. The governing equations are expressed in the tensor notation and the usual summing convention of repeated indices (i, j = 1, 2, 3) is employed.

The deviatoric part of the SGS momentum flux τ_{ij}^d (= $-\nu_t \times \left(\partial\overline{u}_i/\partial x_j + \partial\overline{u}_j/\partial x_i\right)$) and the SGS potential temperature flux σ_j (= $-\nu_t/Pr_t \times \partial\overline{\theta}/\partial x_j$) are modeled by the eddy viscosity and the eddy diffusivity, respectively. Here, ν_t (= $C_k l_\Delta k_{sgs}^{1/2}$) denotes the SGS eddy viscosity; C_k (= 0.0673) the modeling coefficient; l_Δ (= $\Omega^{1/3}$) the filter width; Ω the volume of finite volume (FV) cell; Pr_t (= $\left(1 + 2l/l_\Delta\right)^{-1}$) the turbulent Prandtl number; and l (= l_Δ) the length scale in neutral or unstable ABLs [45]. The SGS TKE k_{sgs} conservation follows the transport equation incorporating atmospheric stability correction [46]

$$\frac{\partial k_{sgs}}{\partial t} + \frac{\partial\left(\overline{u}_i k_{sgs}\right)}{\partial x_i} = -\frac{1}{2}\tau_{ij}^d\left(\frac{\partial \overline{u}_i}{\partial x_j} + \frac{\partial \overline{u}_j}{\partial x_i}\right) + \frac{\nu_t}{\Theta_0 Pr_t}g_i\frac{\partial\overline{\theta}}{\partial x_i} - \left(0.19 + 0.74\frac{l}{l_\Delta}\right)\frac{k_{sgs}^{3/2}}{l} + \frac{\partial}{\partial x_i}\left[\left(\nu + \nu_t\right)\frac{\partial k_{sgs}}{\partial x_i}\right]. \tag{4}$$

2.2. Numerical method

The aforementioned governing equations are solved by the FV method using the Simulator for Wind Farm Applications (SOWFA) [47]. The time integration is carried out by the second-order-accurate backward scheme. In the spatial domain, both the advection and diffusion terms are discretized by the second-order-accurate central differencing. The velocity-pressure coupling in incompressible flows is handled by the pressure-implicit with splitting of operation (PISO) algorithm. After processed by the diagonal incomplete-LU (DILU) preconditioner, the variables $\overline{u}_i$, $\overline{\theta}$, and k_{sgs} are iterated by the bi-conjugate gradient (BiCG) method. The Poisson $\overline{\Pi}$ equation is iterated by the conjugate gradient (CG) method after the geometric agglomerated algebraic multigrid (GAMG) preconditioning. The tolerance of the linear equation system solvers is set at 10^{-6}.

2.3. Computational domain

The (hypothetical) urban surface in this study is fabricated by an 3D array of idealized buildings whose plan area density Λ_p is equal to 25%. These identical rectangular blocks, whose dimensions are W (= 160 m) in width and H (= 80 m) in height, are arranged in a staggered pattern. The computational domain sizes L_x (= $40W$ = 6400 m), L_y (= $40W$ = 6400 m), and L_z (= $25H$ = 2000 m) in the streamwise x, spanwise y, and vertical z directions, respectively (Fig. 1).

Meshes are stretched to balance the modeling accuracy and computational expense. The finest resolution ($\Delta x = \Delta y$ = 10 m and Δz = 5 m) is employed in the bottom near-ground region (z < 160 m) in which each building edge is discretized into at least 16 FV cells to capture the small-scale turbulence [48]. Thereover in the transitional zone (160 m ≤ z < 240 m), the vertical cell size increases gradually from Δz = 5 m to Δz = 10 m over 12 layers. In the CBL core (240 m ≤ z < 800 m), cubic FV cells with Δx_i = 10 m are used. The spatial resolution further relaxes to Δx_i = 20 m (800 m ≤ z < 1200 m) and Δx_i = 40 m (1200 m ≤ z < 2000 m) in the inversion layer. The number of FV cells is about 42 million.

Table 1
Parameters adopted in the current urban CBL LESs. The mean streamwise velocity U_x^h is prescribed at $z = 400$ m and the (surface) vertical potential temperature flux σ_w is prescribed on the rooftops and ground surfaces. The atmospheric stability is measured by the dimensionless length ζ ($= -z_i/L$). Here, z_i is the CBL thickness, L ($= -u_*^3\Theta_0/\kappa\sigma_w|g_3|$) the Obukhov length, Θ_0 (= 300 K) the reference potential temperature, κ (= 0.4) the von Kármán constant, u_* ($= \sqrt{\langle -u'w'\rangle_{z/H=1}}$) the friction velocity, w_* ($= \left(|g_3|\sigma_w z_i/\Theta_0\right)^{1/3}$) the convective velocity scale, and w_m ($= \left(w_*^3 + 5u_*^3\right)^{1/3}$) the combined shear and buoyancy scaling velocity [54]. Convection levels are classified using ζ. Here, $\zeta = 0$ denotes neutral; $0 < \zeta \leq 1$ weak convection with shear dominance ($|L| > z_i$); $1 < \zeta \leq 10$ moderate convection with collective influence from shear and buoyancy ($z_i/10 \leq |L| \leq z_i$); together with $\zeta > 10$ strong convection with buoyancy prevalence ($|L| < z_i/10$).

Case No.	U_x^h (m s^{-1})	σ_w (K m s^{-1})	$\zeta = -z_i/L$	u_* (m s^{-1})	w_* (m s^{-1})	w_m (m s^{-1})	Convection level
1	8.0	0.00	0.00	0.88	0.00	1.51	Neutral
2	8.0	0.02	0.29	0.97	0.87	1.73	
3	8.0	0.05	0.57	1.05	1.18	1.95	Weak
4	8.0	0.10	0.93	1.12	1.48	2.17	
5	6.0	0.15	2.03	0.99	1.70	2.14	
6	4.0	0.15	4.23	0.77	1.70	1.93	Moderate
7	3.0	0.15	6.93	0.66	1.70	1.85	
8	2.0	0.15	13.49	0.53	1.70	1.78	Strong
9	1.0	0.15	48.31	0.34	1.70	1.72	

2.4. Boundary and initial conditions

Periodic boundary conditions (BCs) are enforced to the horizontal extent. The domain top employs a slip velocity BC. No-slip velocity BCs are utilized on wall surfaces. To model unresolved near-wall turbulent processes, the Monin-Obukhov Similarity Theory (MOST) in neutral condition is employed as the wall function in which the surface roughness length is set at 0.1 m [28,49]. Unstable stratification is achieved by prescribing a constant vertical potential temperature flux σ_w on both the rooftops and ground surfaces. It ensures uniform surface heating across horizontal extents, mitigating the potential effects from surface thermal heterogeneity [50]. The range of σ_w adopted (Table 1) is representative of the typical observation on Earth that falls within its Kansas-experiment counterpart [51]. To prevent from any (unintended) heat exchange, zero-gradient BCs of potential temperature are applied to the ground, the lateral building façades, and the domain top. Other variables on the walls and the domain top adhere to zero-gradient BCs.

Initially, a constant (resolved-scale) potential temperature $\overline{\theta}\big|_{t=0} = \Theta_0$ is prescribed from the ground up to $z = 1000$ m. An inversion layer with a constant lapse rate Γ_0 (= 0.05 K m^{-1}) is followed atop. It undergoes artificial warming for offsetting the thermal erosion so as to ensure a rather constant ABL thickness z_i (= 1000 m) throughout the time integration [52]. Moreover, a sponge layer is assigned to the upper domain ($z \geq 1600$ m) to suppress gravity waves.

First of all, the LESs are integrated in time for 20,000 s to achieve statistically stationary states. The output data are then archived for another 20,000 s for post-processing. To mitigate the continuously rising potential temperature during data acquisition (due to the imposed surface heating and absence of heat removal mechanism), a linear detrending technique is applied to the calculation of fluctuating potential temperature [53]. The model validation and turbulence statistics were reported elsewhere [52]. The key parameters employed in the current LESs are summarized in Table 1.

To collect the representative time-series data, three types of vertical profiles are probed in the computational domain. Vertical profiles P1 and P2 are probed at $x = W$ (downstream) and $x = -W$ (upstream), respectively, measuring from the center of the roughness elements. Besides, four vertical x-z planes are inserted evenly in the spanwise direction at $y/L_y = 0.25$, 0.50, 0.75, and 1.00 (Fig. 2). The x-z probing planes are aligned with the vertical x-z symmetry planes of the underlying roughness elements. The LES output data on these profiles and planes are collected at a constant time interval $\Delta t = 0.2$ s to capture the dynamics in a transient manner.

3. Analytical approach

3.1. Amplitude modulation

AM coefficient [18] is employed to investigate the impact of large-scale CBL structures on small-scale turbulent flows. The time-series data are partitioned into large-scale (denoted by subscript L) and small-scale (denoted by subscript S) components. The Taylor hypothesis of frozen turbulence is used to transform time-domain data (frequency f) to spatial-domain data (wavenumber k_x and wavelength λ_x). The magnitude of local mean streamwise velocity $\langle|\overline{u}_x|\rangle_t$ is employed as the convection velocity. Accordingly, the wavenumber and wavelength are defined as $k_x = 2\pi f/\langle|\overline{u}_x|\rangle_t$ and $\lambda_x = \langle|\overline{u}_x|\rangle_t/f$, respectively, where $\langle\xi\rangle_t$ represents the temporal average. This approach differs from previous research that employed $\langle\overline{u}_x\rangle_t$ or Lagrangian approach in selecting the convection velocity [55,56]. The turbulent motion scales are thus more accurately evaluated, especially within the primary recirculation where reverse flows or nearly zero temporal mean velocities often occur [57]. Any given signal χ is decomposed into large-scale χ_L ($\lambda_x > \lambda_c^L$; where λ_c^L is the large-scale cutoff wavelength) and small-scale χ_S ($\lambda_x < \lambda_c^S$; where λ_c^S is the small-scale cutoff wavelength) signals with a Fourier cutoff filter, ensuring distinct energy content in each scale without overlap. Section 4.1 discusses the appropriate λ_c^L setting whose variation is beyond the scope of this study. Other than Section 4.7, in which building-scale AM ($\lambda_x \sim W$) is focused, $\lambda_c^L = \lambda_c^S$ is adopted [18,24].

The Hilbert transform [58] is adopted to obtain the envelope of small-scale fluctuation $E(\psi_S')$, where the prime $'$ denotes the deviation from the temporal mean. This envelope not only reflects the modulation from large-scale signals but also the minor variations from small-scale ones. To extract the large-scale modulation from small-scale variation, the envelope is subjected to a high-pass filter at the cutoff wavelength λ_c^L. A filtered envelope $E_L(\psi_S')$ is yielded that exclusively represents the modulation of small-scale fluctuations by the large-scale signals.

The modulation is measured by the correlation coefficient between the large-scale modulating signal φ_L and the large-scale envelope $E_L(\psi_S')$ of the small-scale carrier signal ψ_S

$$R_{\varphi_L,\psi_S}(x_i,\Delta t) = \left\{ \frac{\left\langle \varphi_L'(x_i,t) \times E_L'\left(\psi_S'(x_i,t-\Delta t)\right)\right\rangle}{\sqrt{\left\langle {\varphi_L'}^2(x_i,t)\right\rangle}\sqrt{\left\langle {E_L'}^2\left(\psi_S'(x_i,t-\Delta t)\right)\right\rangle}} \right\}_{\mathfrak{R}}. \quad (5)$$

Here, the angle brackets $\langle\xi\rangle$ and the curly brackets $\{\xi\}_{\mathfrak{R}}$ denote the ensemble average and the averaging over repeating units, respectively. As such, the AM coefficient is reduced to $R_{\varphi_L,\psi_S}(z,\Delta t)$ along the

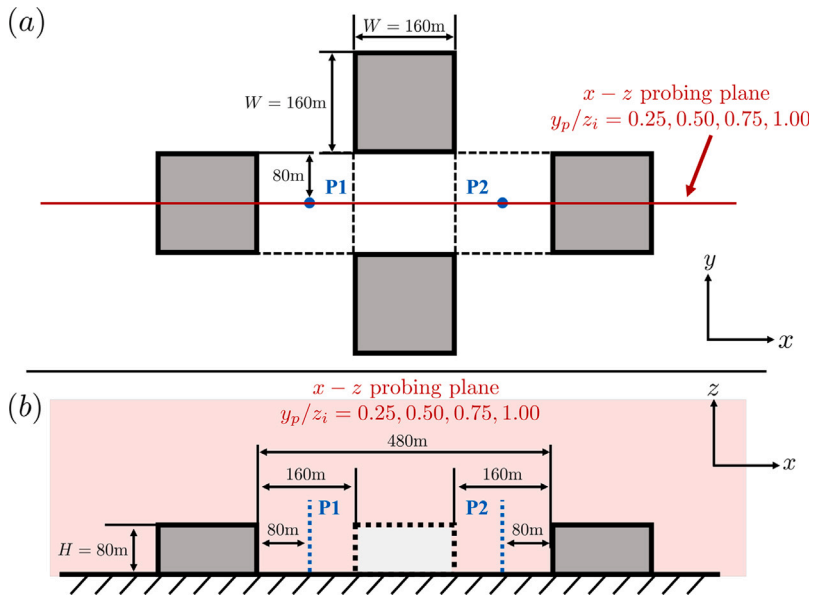

Fig. 2. (a) Plan and (b) elevation views of the array of roughness elements together with the probe locations of vertical profiles P1 and P2.

profiles P1 and P2. Similarly, on the vertical x-z sample plane, it is reduced to $R_{\varphi_L,\psi_S}(x,z,\Delta t)$. The time lag Δt is included to analyze the phase information of AM. A non-zero Δt indicates either the large-scale modulating signal φ_L leads ($\Delta t < 0$ s) or lags ($\Delta t > 0$ s) the small-scale carrier signal ψ_S. This paper primarily discusses $\Delta t = 0$ s. The analysis of non-zero Δt is confined to Section 4.8 that specifically addresses the phase relationship between modulating and carrier signals in different ABL stability.

In this study, we consider both large-scale streamwise u_L and vertical w_L velocities as potential modulating signals for calculating the AM coefficient. Previous studies have shown that these two components can modulate small-scale turbulence in unstable ABLs [24,39]. The small-scale velocity components (u_S, v_S, w_S), potential temperature (θ_S), vertical momentum flux ($(u'w')_S$, denoted as uw_S), and heat flux ($(w'\theta')_S$, denoted as $w\theta_S$) are considered carrier signals. They are crucial for the land-surface parameterization in NWP models [59].

Statistically, a positive AM coefficient suggests that large-scale accelerating (or upward) flows have a more pronounced impact on small-scale turbulence generation. Otherwise, their decelerating (or downward) counterparts have a more pronounced impact on small-scale turbulence suppression. This study focuses on single-point modulation that is reliable for AM estimate in both isothermal and buoyant flows [18,24].

To assess the cumulative impact of large-scale modulation on canopy-level (the combination of UCL and RSL) turbulence from the probes P1 and P2, an integrated AM coefficient

$$\mathcal{R}_{\varphi_L,\psi_S} = \frac{1}{z_{\mathrm{RSL}}}\int_0^{z_{\mathrm{RSL}}} R_{\varphi_L,\psi_S}(z,\Delta t=0)\, dz \tag{6}$$

is introduced. Here, the RSL height is set at $z_{\mathrm{RSL}} = 1.5H$ which is widely recognized in literature [34,35].

3.2. Scale-decomposed skewness

To investigate the multi-scale interactions among different scales, the scale-decomposed skewness of full-scale streamwise u

$$\begin{aligned}\widetilde{u'^3} &= \frac{\langle u'^3\rangle}{\langle u'^2\rangle^{3/2}} = \frac{\left\langle (u'_L+u'_S)^3\right\rangle}{\langle u'^2\rangle^{3/2}} \\ &= \frac{\langle u'^3_L\rangle}{\langle u'^2\rangle^{3/2}} + 3\frac{\langle u'_L u'^2_S\rangle}{\langle u'^2\rangle^{3/2}} + 3\frac{\langle u'_S u'^2_L\rangle}{\langle u'^2\rangle^{3/2}} + \frac{\langle u'^3_S\rangle}{\langle u'^2\rangle^{3/2}} \\ &= \widetilde{u'^3_L} + 3\widetilde{u'_L u'^2_S} + 3\widetilde{u'_S u'^2_L} + \widetilde{u'^3_S}\end{aligned} \tag{7}$$

and vertical w

$$\begin{aligned}\widetilde{w'^3} &= \frac{\langle w'^3\rangle}{\langle w'^2\rangle^{3/2}} = \frac{\left\langle (w'_L+w'_S)^3\right\rangle}{\langle w'^2\rangle^{3/2}} \\ &= \frac{\langle w'^3_L\rangle}{\langle w'^2\rangle^{3/2}} + 3\frac{\langle w'_L w'^2_S\rangle}{\langle w'^2\rangle^{3/2}} + 3\frac{\langle w'_S w'^2_L\rangle}{\langle w'^2\rangle^{3/2}} + \frac{\langle w'^3_S\rangle}{\langle w'^2\rangle^{3/2}} \\ &= \widetilde{w'^3_L} + 3\widetilde{w'_L w'^2_S} + 3\widetilde{w'_S w'^2_L} + \widetilde{w'^3_S}\end{aligned} \tag{8}$$

velocities are studied [60]. The cross-scale terms $\widetilde{u'_L u'^2_S}$ and $\widetilde{w'_L w'^2_S}$ signify the influence of large-scale signals on small-scale turbulence intensities. Likewise, $\widetilde{u'_S u'^2_L}$ and $\widetilde{w'_S w'^2_L}$ reflect the influence of small-scale signals on large-scale turbulence intensities. Previous research primarily focused on the scale-decomposed skewness of u, revealing a notable connection between $\widetilde{u'_L u'^2_S}$ and the AM coefficient R_{u_L,u_S} [30]. Their relationship was also derived theoretically that is applicable to any stationary signals [31]. Likewise, $\widetilde{w'_L w'^2_S}$ is considered indicative of the potential modulation by large-scale vertical velocity in this study.

3.3. Wavelet analysis

Wavelet analysis is employed in this study to detect the small-scale turbulence excitation embedded in a broad spectrum. It enables the breakdown of signals into their respective time and frequency components to identify the predominant modes along with their temporal behavior. Such capability renders wavelet analysis an ideal tool for investigating coherent structures which are non-stationary, intermittent, or non-Gaussian [61,62].

The wavelet coefficient

$$T_w(t,t_s) = \int_{-\infty}^{+\infty} \chi(\eta)\,\Psi^*\left(\frac{\eta - t}{t_s}\right) d\eta \tag{9}$$

is calculated by convoluting a time series $\chi(t)$ with the scaled mother wavelet Ψ where the asterisk $*$ denotes the complex conjugate [61].

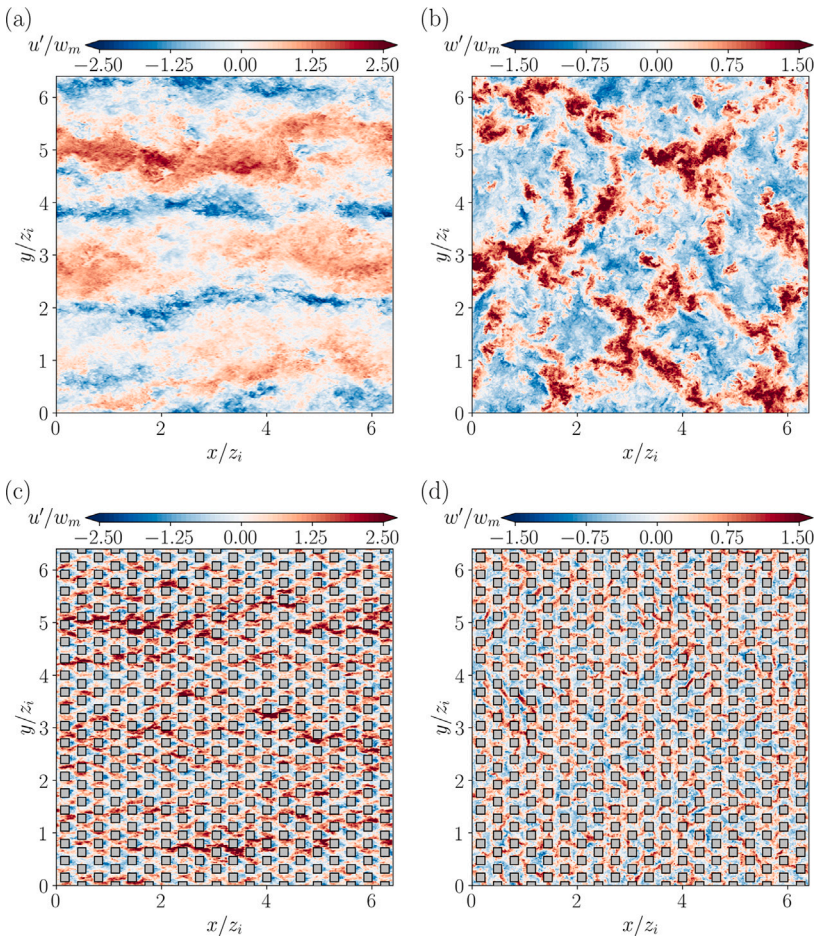

Fig. 3. Horizontal slices of instantaneous velocity fluctuations u_i' normalized by the combined shear and buoyancy scaling velocity w_m: (a), (c) streamwise velocity fluctuation u' at $\zeta = 0.57$ (weak convection) and (b), (d) vertical velocity fluctuation w' at $\zeta = 48.31$ (strong convection). Two heights are considered: (a), (b) within mixed layers at $z/z_i = 0.4$ ($z/H = 5$) and (c), (d) within urban canopy layers at $z/z_i = 0.06$ ($z/H = 0.75$).

The time-scale parameter t_s stretches or compresses the wavelet scale while the displacement parameter t shifts the wavelet along the time axis. The complex Morlet wavelet

$$\Psi\left(\frac{\eta - t}{t_s}\right) = e^{i\omega_0(\eta-t)/t_s} e^{-\frac{1}{2}\times|(\eta-t)/t_s|^2} \tag{10}$$

is selected as the mother wavelet because of its superior frequency resolution. The dimensionless frequency ω_0 is kept at 6, balancing the trade-off between time and frequency localization [24]. The (time-localized) wavelet PSD [61]

$$\Phi_w(t, t_s) = \frac{\left|T_w\left(t, t_s\right)\right|^2}{t_s}. \tag{11}$$

is calculated to compare the fluctuation intensity with various scales t_s at specific time t.

4. Result and discussion

4.1. Flow characteristics

Fig. 3 contrasts the influence of CBL structures on UCL ($z/H < 1$; [63]) flows calculated by the LESs. In weak convection ($\zeta = 0.57$), convective rolls are observed within the CBL core (Fig. 3a). They are characterized by streamwise-elongated deceleration (intense updraft) and widespread acceleration (weak downdraft). In contrast, strong convection ($\zeta = 48.31$) leads to the formation of narrow, plume-like updraft and compensatory downdraft in the CBL (Fig. 3b) whose distortion by prevailing winds is minimal.

The UCL flows at the ABL bottom (Fig. 3c and d), for instance, the strong acceleration or updraft, are modified significantly by the CBL core structures (Fig. 3a and b) that is evidenced by their alike flow patterns. However, the presence of explicitly resolved roughness elements distorts these imprints, partitioning them into smaller segments, producing small-scale turbulent flows compared with the (large-scale) ones in the mixed layers. Notably, the wakes after buildings, which are characterized by reversing flows adjacent to leeward walls, are prominent under shear-dominant conditions.

Different from previous studies [24,34,36], immersing roughness elements in unstable ABLs complicates the selection of filter length in this study. The premultiplied PSDs of the streamwise and vertical velocities of two cases of urban CBLs are compared in Fig. 4. Apparently, large-scale convective rolls and plume-like structures occur in the weak convection ($\zeta = 0.57$) and the strong convection ($\zeta = 48.31$), respectively.

Given the aerodynamic effect of roughness elements was modeled in (previous) canonical TBLs, two prominent peaks are evident in the premultiplied PSD of streamwise velocity fluctuation u' [18]. The inner and outer peaks are separated discernibly in the logarithmic region [24]. Once the roughness elements are resolved explicitly, on the contrary, the energy varies continuously in the spectral space in the wall-normal distance [64], blurring the (distinct) outer peak (Fig. 4a).

Evidently, small-scale turbulence is mainly induced by buildings at the canopy level. The streamwise velocity premultiplied PSD in weak convection ($\zeta = 0.57$) is concentrated around wavelength $\lambda_x = W$ which is (much) shorter than z_i (Fig. 4a). These findings align with the well-established notion that the sizes of buildings and eddies are

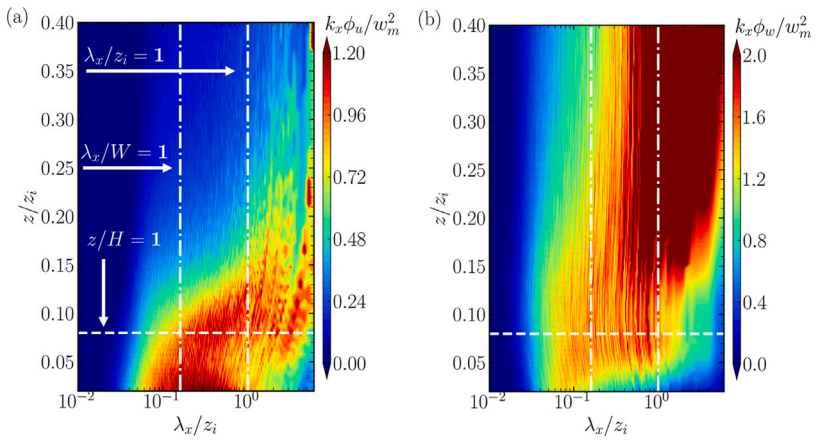

Fig. 4. Shaded-contours of the premultiplied PSD for (a) streamwise $k_x\phi_u/w_m^2$ at ζ = 0.57 (weak convection) and (b) vertical $k_x\phi_w/w_m^2$ at ζ = 48.31 (strong convection) velocity fluctuations measured along profile P2.

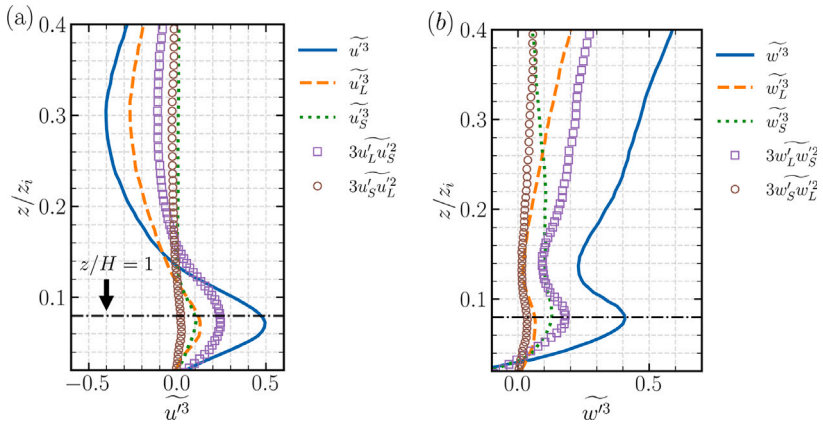

Fig. 5. Total and scale-decomposed skewness of (a) streamwise u at ζ = 0.57 (weak convection) and (b) vertical w at ζ = 48.31 (strong convection) velocities measured along profile P2.

comparable within UCLs [65]. In contrast, in the mixed layer aloft ($z/H > 1.5$), the streamwise velocity fluctuation u' is notably affected by the elongated convective rolls. Hence, most of the energy resides at wavelength λ_x exceeding z_i.

Although the size of UCL vertical velocity fluctuation w' is shorter than the inversion height z_i, thermal plumes tend to accumulate energy at a longer wavelength λ_x in the strongly unstable mixed layer (ζ = 48.31; Fig. 4b). This demarcation by z_i distinguishes (small-scale) UCL turbulence from (large-scale) CBL structures. It holds under both shear (ζ = 0.57) and buoyancy (ζ = 48.31) dominant conditions (Fig. 4). In line with previous studies [24,34,36], $\lambda_c^L = z_i$ is an appropriate cutoff wavelength being adopted in this study.

4.2. Scale-decomposed skewness

To examine the modulation of small-scale turbulence by u_L and w_L together with the coherent structures in urban CBLs, the total and scale-decomposed skewness of velocities (RHS of Eqs. (7) and (8)) in the wall-normal direction are plotted (Fig. 5). Unless in the proximity of the ground surface, secondary flow is barely induced upstream a roughness element [34]. The plan area density Λ_p of the current configuration equals 25% so UCL secondary flows are insignificant. The results along the profile P2 are therefore adopted to display the AM in urban CBLs.

In the shear-dominant regime ζ = 0.57 (Fig. 5a), the large-scale streamwise velocity fluctuation u_L' contributes most to the skewness $\widetilde{u'^3}$ in the mixed layers where convective rolls prevail [20,52]. These roll-type CBL structures also leave footprints as indicated by $\widetilde{u_L'^3}$ in the UCL which is comparable to its small-scale counterpart $\widetilde{u_S'^3}$. In contrast, $\widetilde{u_S'^3}$ is negligible unless in UCLs where eddies are fragmented into smaller ones during their passage through [66]. The scale-interaction term $3\widetilde{u_L'u_S'^2}$ emerges as a crucial component in the UCLs that remains non-negligible in the mixed layer. It in turn exemplifies the AM of small-scale streamwise turbulence intensity $u_S'^2$ by large-scale convective rolls u_L'.

Thermal plumes in the buoyancy-dominant regime ζ = 48.31, which are driven by the vertical flows, are the major modulators in both UCLs and mixed layers. Obviously, the scale-interaction term $3\widetilde{w_L'w_S'^2}$ is the primary contributor to the total skewness of vertical velocity $\widetilde{w'^3}$ (Fig. 5b), illustrating the uplifting of small-scale vertical turbulence intensity $w_S'^2$ (by large-scale buoyancy-induced vertical flows w_L'). The notable contributions from the cross-scale terms $3\widetilde{u_L'u_S'^2}$ (Fig. 5a) and $3\widetilde{w_L'w_S'^2}$ (Fig. 5b) affirm the potential modulation by u_L' and w_L' in urban CBLs, paving the way for further exploration of scale interactions based on AM coefficient (Eq. (5)).

4.3. Stability dependence of AM coefficients

Fig. 6 displays the vertical variation of the AM coefficients R_{u_L,u_S} and R_{w_L,u_S} in different atmospheric stability that exclusively examines u_S' as the carrier signal. In the neutral case ζ = 0.00, R_{u_L,u_S} is positive at the canopy level that is peaked at the UCL top (maximum

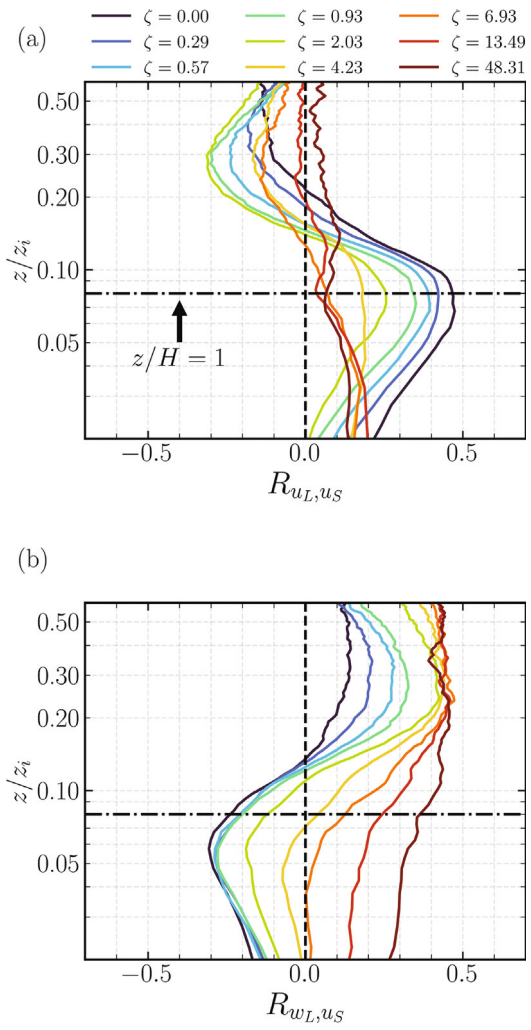

Fig. 6. Vertical profiles of amplitude modulation coefficients: (a) R_{u_L,u_S} and (b) R_{w_L,u_S} measured along profile P2 under various stability conditions. The vertical dashed line denotes the zero-discriminant line.

R_{u_L,u_S} is around 0.5). Hence, the large-scale accelerating (decelerating) streamwise flows are prone to excite (quieten) small-scale streamwise turbulence in the UCLs. These findings align with those in previous studies of isothermal TBLs over urban-like rough surfaces, demonstrating the substantial influence of large-scale coherent structures [34,36,37]. Over the UCL, R_{u_L,u_S} declines with increasing elevation, zero-crossing at the lowest level of the mixed layers ($z/z_i = 0.2$). Thereover, the large-scale decelerating (accelerating) flows primarily stimulate (quell) the small-scale streamwise turbulence locally, consistent with those in canonical TBL scenarios [18].

Once unstable convection is applied, R_{u_L,u_S} decreases near the UCLs. Moreover, the zero-crossing descends with increasing ζ (more unstable) so the AM is weakened. This pattern could be attributed to the enhanced buoyancy in UCLs and the TKE production in stronger convection [25].

Interestingly, R_{u_L,u_S} is more negative in the mixed layers when the ABL is switched from neutral ($\zeta = 0.00$) to moderately unstable ($\zeta = 2.03$). It is in turn suggested that, in the outer layers, the influence of large-scale, decelerating flows on small-scale turbulence is augmented in buoyancy-induced updrafts. Although the modulation of u_S by u_L was reported monotonically diminishing across the CBLs with increasing ζ elsewhere [24], the aforementioned discrepancy could stem from the transition of large-scale coherent structures in response to thermals. Notably, the least convective condition in Salesky and Anderson [24] was $\zeta = 3.1$ that surpassed the peaked coherence of convective rolls (maximum coherence state at $\zeta = 1.08$) reported in literature [20].

Conversely, this study covers the CBL stability under which convective rolls are initiated, attaining maximum coherence. These conditions align with the scenarios where $\left|R_{u_L,u_S}\right|$ monotonically increases with increasing ζ in the mixed layers. Specifically, as ζ rises from 2.03 (moderate convection), convective rolls transition to less coherent, patch-like structures [26] and $|R_{u_L,u_S}|$ declines [24]. This observation signifies the importance of transitions of coherent structures to CBL large-scale modulation. From a statistical perspective, the negative u'_L (deceleration) within convective rolls arouses small-scale streamwise turbulence in CBL cores. On the contrary, its positive counterpart (acceleration) inhibits such scale interaction. This characteristic modulation is most pronounced when the convective rolls are at their peaked coherence.

In neutral stability ($\zeta = 0.00$), R_{w_L,u_S} is negative within the UCLs whose magnitude is slightly less than that of R_{u_L,u_S}. Hence, large-scale downdrafts excite small-scale UCL flows, and vice versa. The role of w_L has been overlooked in previous isothermal studies [34,36,37]. In fact, the modulation of u_S by w_L could be attributed to the tight, negative correlation between the streamwise u and vertical w flows [52]. This study further diagnoses the processes, unveiling the momentum transport mechanism in a multi-scale manner.

In the mixed layers, R_{w_L,u_S} increases monotonically with increasing ζ (more unstable). The buoyancy-induced, large-scale updrafts (downdrafts) w'_L enhance (suppress) small-scale streamwise fluctuations u'_S in CBL cores [24]. This could be interpreted as the results of the enhanced buoyancy-driven thermals which are originated from the hot ground surfaces. An intriguing transition in R_{w_L,u_S} is observed with varying ζ: it switches from negative to positive when the ABL is evolving from neutral to convective. The negative AM coefficient R_{w_L,u_S} in neutral and weak convection implies that the downdrafts within streaks or convective rolls predominantly trigger streamwise turbulence. With increasing ζ (more unstable), on the contrary, UCL small-scale turbulence excitation (suppression) are predominantly driven by large-scale updrafts (downdrafts), mirroring the processes observed in CBL cores.

The results above underscore the pivotal role of large-scale CBL coherent structures, particularly their stability-dependent transitions from streaks (neutral) to convective rolls (weak convection), and thermal plumes (strong convection), influencing turbulent UCL processes. Furthermore, the current findings are consistent with those of prior research focusing on vertical momentum fluxes using conditional statistics [52], lending additional credence to our anaylsis.

4.4. Wavelet analysis

Juxtaposing the time series of large-scale variables φ_L with the premultiplied wavelet PSD depicts the intuitive AM phenomena (Fig. 7). They are the P2-profile data sampled at $z/H = 0.75$ that represent the UCL processes. The onset of energetic, small-scale streamwise turbulence is evidenced by the pronounced brightness with shorter wavelength λ_x in the PSD shaded contours.

In weak convection ($\zeta = 0.57$; Fig. 7a), where convective rolls exist, a notable correlation emerges among strong small-scale streamwise velocity fluctuations u'_S, large-scale downdrafts ($w'_L < 0$), and concurrent accelerations ($u'_L > 0$). Along with the spectral peaks at small-scale streamwise velocity fluctuation $f\Phi_w/\sqrt{\langle u'^2\rangle}$, intense, large-scale envelope of small-scale streamwise turbulence $E'_L(u'_S)$ coincides with the large-scale events u'_L and w'_L (at dimensionless time $t \times w_m/z_i \approx$ 31.2, 33.0, and 35.2, then again from 37.8 to 38.4; orange arrows), suggesting the multi-scale turbulence excitation. Their noticeable time lags warrant elaboration in the subsequent sections.

In contrast, small-scale streamwise turbulence is clearly absent from the time period $33 \le t \times w_m/z_i \le 35$ (orange band). In this interval, the profile P2 is immersed in large-scale updrafts ($w'_L > 0$) or decelerating flows ($u'_L < 0$) where $E_L(u'_S)$ falls below its mean. This finding is in line

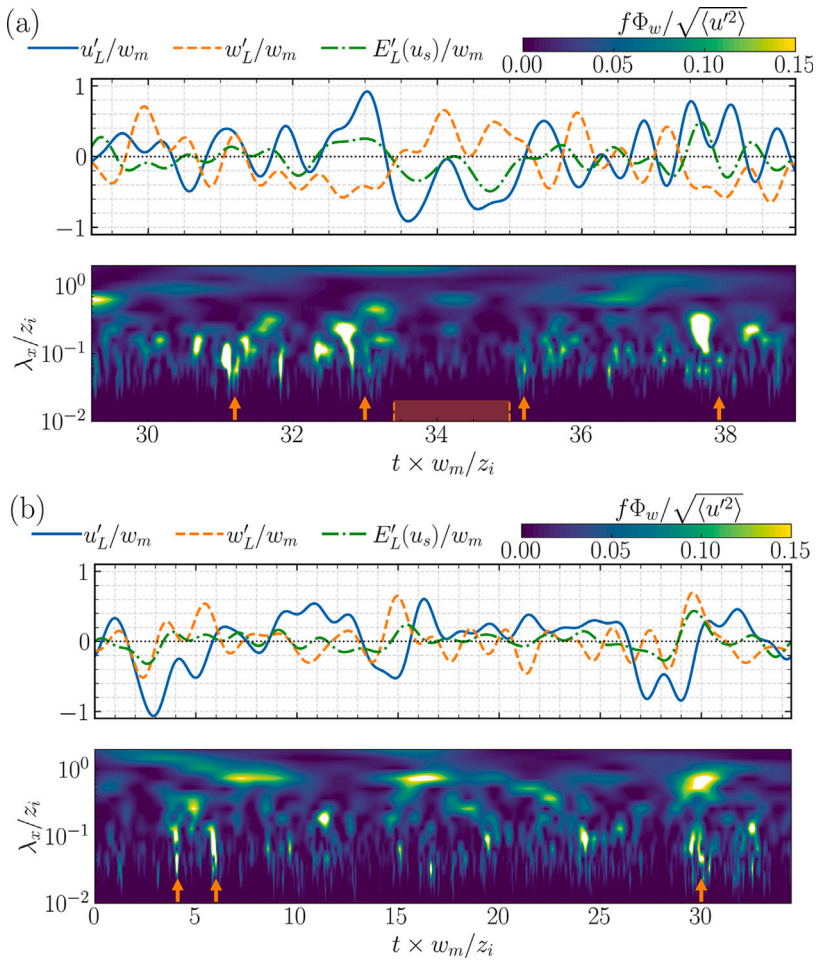

Fig. 7. Time series of the dimensionless large-scale streamwise u'_L and vertical w'_L velocity fluctuations, the large-scale envelope of small-scale streamwise velocity fluctuation $E'_L(u'_S)$, together with the dimensionless premultiplied wavelet PSD of the streamwise velocity fluctuation $f\Phi_w/\sqrt{\langle u'^2\rangle}$ (Eq. (11)) for (a) ζ = 0.57 (weak convection) and (b) ζ = 48.31 (strong convection). Profile P2 data are sampled at z/H = 0.75. The orange markers in the scalogram refer to the instants mentioned in the text. The dotted line is the zero-discriminant line.

with the AM analysis above. It substantiates that large-scale updrafts or decelerations suppress the small-scale streamwise turbulence intensity within UCLs.

In strong convection (ζ = 48.31; Fig. 7b), it is evident that large-scale updrafts ($w'_L > 0$) predominantly contribute to the streamwise velocity fluctuation u'_S. This is clearly illustrated by $E'_L(u'_S)$ and the PSD at $t \times w_m/z_i \approx$ 4.1, 6.0, and 30.0 (orange arrows). Such findings align with the positive AM coefficient $R_{w_L,u_S} > 0$ observed within the UCL (Fig. 6b). Because of their nearly independent temporal evolution, the correlation between u'_L and w'_L is much weakened in strong convection than that in weak convection. As a result, the large-scale updrafts ($w'_L > 0$) serve as the primary modulators. In contrast, no direct correlation between u'_L and u'_S is discernible either from $E'_L(u'_S)$ or the wavelet PSD. The results from AM analysis are corroborated by wavelet analysis, reinforcing the interaction between large-scale and small-scale turbulence in urban CBLs.

4.5. Integrated AM coefficient

The dependence of integrated AM coefficients $\mathcal{R}_{u_L,\psi_S}$ and $\mathcal{R}_{w_L,\psi_S}$ on ABL stability is illustrated (Fig. 8). Here, all small-scale carrier signals ψ_S discussed in Section 2 are considered to explore the overall AM within UCLs. It is observed that small-scale signals are influenced by the large-scale velocities in the RSLs beneath z_{RSL}. Their coupling is a function of ABL stability.

Typically, $\mathcal{R}_{u_L,\psi_S}$ decreases with increasing ζ (more unstable; Fig. 8a) that is attributed to the collective effect of buoyancy and the diminishing coherence of streamwise turbulence as elaborated above. Notably, from neutral condition (ζ = 0.00) to moderate convection (ζ = 2.03), the correlation coefficients $\mathcal{R}_{u_L,uw_S}$ and $\mathcal{R}_{u_L,w\theta_S}$ exceed those of their first-order counterparts $\mathcal{R}_{u_L,u_S}, \mathcal{R}_{u_L,w_S}, \mathcal{R}_{u_L,\theta_S}$ except $\mathcal{R}_{u_S,w\theta_S}$ in neutral condition. This observation underscores the importance of the modulation of vertical fluxes by large scales and the influence of ABL stability. These key variables in land-surface parameterizations are more profoundly influenced by large-scale CBL structures, whose roles, however, are mostly neglected nowadays.

As reflected by $\mathcal{R}_{w_L,\psi_S}$, the influence from large-scale vertical flows progressively increases with increasing ζ (more unstable; Fig. 8b). As previously mentioned, beneath the RSL height $z/H \leq$ 1.5, $\mathcal{R}_{w_L,\psi_S}$ switches from negative (shear dominance) to positive (buoyancy dominance). The former suggests the roles of large-scale downdrafts which are embedded in the elongated streaks or convective rolls, generating small-scale UCL turbulence. The latter suggests that the primary modulators switch to buoyancy-induced updrafts/downdrafts in strong convection. Compared with the momentum-related quantities, intense fluctuations of small-scale potential temperature θ'_S and vertical heat flux $w\theta_S$ are more likely to be excited by plume-like updrafts.

The integrated AM coefficient $\mathcal{R}_{\varphi_L,\psi_S}$ indicates a tight dependence of UCL transport processes on ABL stability (Fig. 8). Traditionally, large-scale streamwise velocity u_L was considered a primary modulator of near-surface turbulence in neutral UCLs [34,37] as well as a major

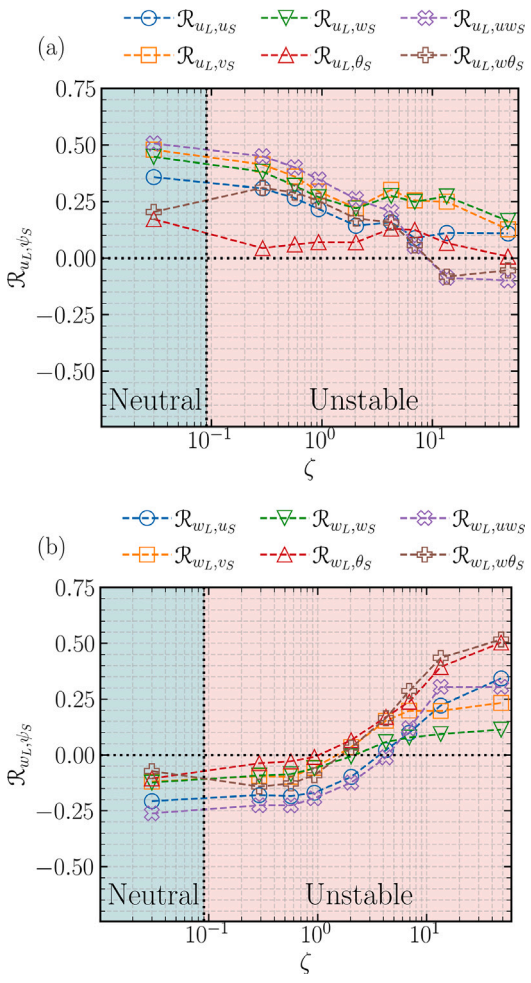

Fig. 8. Dependence of the canopy-level-integrated amplitude modulation coefficients on ABL stability at profile P2. (a) $\mathcal{R}_{u_L,\psi_S}$ and (b) $\mathcal{R}_{w_L,\psi_S}$ The horizontal dashed line indicates the zero-discriminant line. For comparison purposes, the results in neutral case $\zeta = 0.00$ are also depicted with a pseudo-non-zero stability parameter.

input for predictive models [38]. However, its role diminishes with increasing ζ (more unstable) in CBL. Hence, the theory developed in neutral ABL must be interpreted cautiously in unstable ABL. Further investigations are necessary.

The large-scale vertical velocity w_L is also highlighted as a potential modulating signal in this study. It exhibits a non-negligible modulation level in both shear and buoyancy dominance. Specifically, switching CBL structures from convective rolls to thermal plumes modifies the (mechanism of) AM in urban CBLs as reflected by the stability dependence of $\mathcal{R}_{w_L,\psi_S}$. This transition, however, shifts the w_L-based AM coefficient from negative to positive. Such zero-crossing would lead to misconceptions about AM in moderate convection especially in those regions where $\mathcal{R}_{w_L,\psi_S} \approx 0$. An approach employing both u_L and w_L is suggested instead for the development of predictive models in non-isothermal flows.

4.6. Building wakes

Shaded contours of $R_{\varphi_L,\psi_S}(x, z, \Delta t = 0)$ are depicted to elucidate the influence of individual buildings on the AM within UCLs (Fig. 9). They are the ensemble average encompassing all the repeating units on all the x-z sample planes. Specifically, R_{u_L,uw_S} in weak convection ($\zeta = 0.57$) and R_{w_L,uw_S} in strong convection ($\zeta = 48.31$) are depicted. Vertical momentum flux uw_S is plotted as the carrier signal hereafter due to the stronger susceptibility to modulation than its velocity components

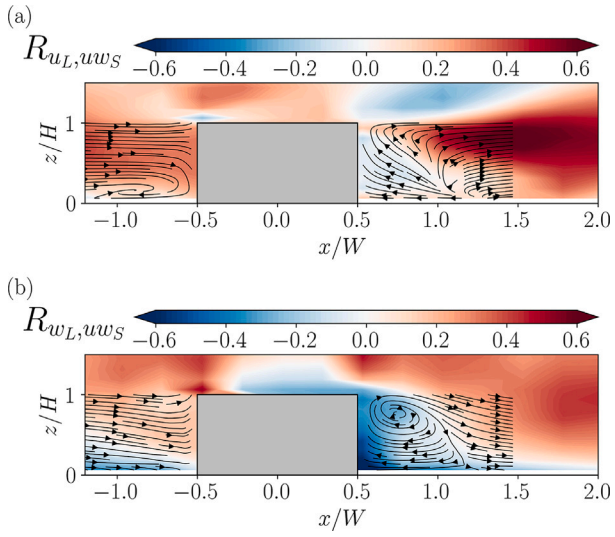

Fig. 9. Shaded contours of ensemble-averaged amplitude modulation coefficients (a) R_{u_L,uw_S} at $\zeta = 0.57$ (weak convection) and (b) R_{w_L,uw_S} at $\zeta = 48.31$ (strong convection) on the vertical (x-z) symmetry plane of the roughness element (colored in gray). Also shown are the time-averaged streamlines (arrows). The origin of the coordinate is reset at the bottom center of the roughness element.

(Fig. 8). It also plays a crucial role in land-surface parameterization as well as drag calculation.

Characteristic mean flow patterns around buildings are discernible from the streamlines in both ABL stabilities. Frontal stagnation adjacent to the windward wall and the primary recirculation behind the leeward wall are noticeable. A key distinction is the presence of a rear vortex [67] which is only observed in strong convection ($\zeta = 48.31$; Fig. 9b) but not in weak convection ($\zeta = 0.57$; Fig. 9a). It is attributed to the different streamwise turbulence intensities $u'u'$ in the approaching flow [57] which is higher in weak convection [52].

Apart from the mean flows, distinctive behaviors are observed under different stabilities. In weak convection ($\zeta = 0.57$), R_{u_L,uw_S} is peaked at the roof-level shear layer. This peak highlights the top-down influence of large-scale structures [15,23] on canopy-level small-scale turbulence through their interactions with roughness elements.

Conversely, in strong convection ($\zeta = 48.31$), plume-like updrafts trigger small-scale UCL turbulence. The AM coefficient R_{w_L,uw_S} thus displays a more uniform spatial distribution. Unlike weak convection, strong AM is absent from the shear layers. This observed homogeneity is caused by the diminishing interactions between large-scale vertical flows and roughness elements. Hence, it is a consequence of the 'bottom-up' mechanism in strong convection in which updrafts are initiated by hot surfaces [23,68]. In this connection, plumes rise more rapidly than horizontal displacement ($w_* > U_x^h$), weakening their interactions with roughness elements [52].

Regardless of the ABL stability, the AM coefficients R_{u_L,uw_S} is negative in the recirculation on the building leeward side (Fig. 9). Besides, the negative R_{w_L,uw_S} above UCLs is attributed to the diminishing interaction between the rooftop flows and the hot plumes originating from the heated ground surfaces. It was also highlighted elsewhere on the impact of building-induced local flows by comparing the single-point and two-point AM coefficients [34]. The current results demonstrate the dominance of local dynamics under various ABL stabilities.

The influence of building-induced wakes on AM is elucidated by examining $\mathcal{R}_{\varphi_L,\psi_S}$ at probe P1 within the primary recirculation (Fig. 10). In contrast to those at probe P2 (Fig. 8), the AM coefficients at probe P1 are generally smaller in magnitudes. Thus, the small-scale turbulent processes in a building wake are less modulated by the large-scale velocities. Moreover, compared with that at P2, the stability dependence

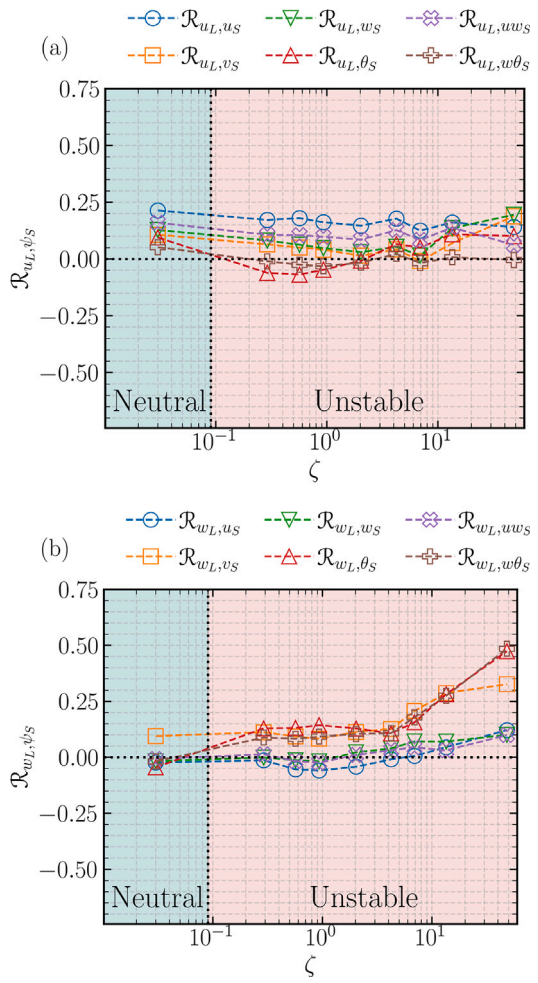

Fig. 10. Dependence of the canopy-level-integrated amplitude modulation coefficients on ABL stability at profile P1. (a) $\mathcal{R}_{u_L,\psi_S}$ and (b) $\mathcal{R}_{w_L,\psi_S}$. The format is the same as that in Fig. 8.

of $\mathcal{R}_{\varphi_L,\psi_S}$ at P1 shows a less coupling that remains nearly constant across most stability regimes. The influence of large-scale plumes on small-scale turbulent processes is solely noticeable in spanwise velocity or temperature-related variables (Fig. 10b). These observations reveal the minor roles of large-scale CBL structures in the AM at probe P1, signifying the predominance of local dynamics.

Comparing the AM coefficients at probes P1 and P2, the spatial dependence of $\mathcal{R}_{\varphi_L,\psi_S}$ suggests the importance of both the geometry and heterogeneity of roughness elements. For example, skyscrapers could induce elongated flow structures downstream [62]. Under this circumstance, predictive models of UBLs should be employed cautiously to assess small-scale dynamics based on outer-layer flows, especially if the target areas are in close proximity to buildings.

4.7. AM on building-scale turbulence

While λ_c^L is kept at z_i, the influence of λ_c^S on $\mathcal{R}_{\varphi_L,\psi_S}$ in weak (ζ = 0.57) and strong (ζ = 48.31) convections is depicted in Fig. 11. For weak convection, decreasing λ_c^S from z_i leads to increasing $\mathcal{R}_{u_L,\psi_S}$. As such, small-scale turbulent processes are more influenced by large-scale structures in UCLs. This behavior aligns with the findings in near-neutral ASLs above sand-grain roughness, where an almost constant log-linear scaling precedes the peaked AM coefficient with diminishing λ_c^S [69]. In scenarios with explicitly resolved buildings, reducing λ_c^S beyond building width W results in a scaling slope (k_s = −0.20) steeper than that for $\lambda_c^S > W$ (k_s = −0.05; Fig. 11a). A comparable trend is observed in $\mathcal{R}_{w_L,\psi_S}$, albeit with less steep scaling slopes (Fig. 11b). These results suggest a stronger modulation of building-scale turbulent processes by convective rolls than that by other scales. This assertion is further corroborated by the wavelet premultiplied PSD (Fig. 7a) at $t \times w_m/z_i$ = 31.2, where building-scale streamwise turbulence ($\lambda_x \leq W$) is mainly excited by large-scale accelerations. In contrast, intermediate-scale turbulence ($W < \lambda_x \leq z_i$) remains relatively calm.

In spite of the minor effect on the full spectrum of small-scale turbulence ($\lambda_x < z_i$; Fig. 8a), notable interactions between resolved roughness elements and patch-like streamwise motions in strong convection are observed (Fig. 11b). The latter modulates the building-scale turbulence as quantified by the increase in $\mathcal{R}_{u_L,\psi_S}$ with decreasing λ_c^S that reaches its maximum for $\lambda_c^S < W$. In this context, accelerating and decelerating patches enhance and suppress, respectively, building-scale turbulence. In contrast to weak convection (ζ = 0.57), the scaling slope is less modified by resolved elements in strong convection (ζ = 48.31). Moreover, the major decrease in $\mathcal{R}_{w_L,\psi_S}$ suggests that the excitation (suppression) of building-scale turbulence is less influenced by large-scale updrafts (downdrafts). Unlike their streamwise counterparts, these large-scale vertical structures tend to modulate intermediate-scale turbulence, rather than directly affecting the building-scale dynamics.

In short, building-scale turbulence is more susceptible to the modulation by large-scale (streamwise) motions in weak or strong convection (Fig. 11). This finding underscores the role of CBL structures in wind-building interactions and the necessity of including their influence on land-surface parameterization of urban areas.

4.8. Phase relationship

The phase information of the AM coefficients are plotted in Fig. 12. Here, the modulating signal is w_L owing to its key role in UCL AM in unstable ABL. Time-series data are collected at probe P2 within the UCLs at z/H = 0.75, making it an ideal site for applying predictive models. The phase $\Delta t^{\pm}_{\text{peak}}$ represents the time difference at which the magnitude of R_{w_L,uw_S} attains its maximum, and the superscript ± indicates whether Δt is positive (+; lags) or negative (−; leads).

In weak convection (ζ = 0.57), $R_{w_L,uw_S}(\Delta t)$ reaches its negative peak concurrently with $\Delta t^{+}_{\text{peak}}$. The large-scale envelope of the small-scale signal $E'_L(uw_S)$ precedes the large-scale vertical flows w'_L in the time domain (spatial leads). This phenomenon has been extensively observed in neutral TBLs [61]. However, the underlying mechanisms are yet elucidated so further investigation warrants. Our findings corroborate the existence of such phenomenon in the UCLs of weak convection. Moreover, the organization of convective rolls merely impacts the phase of the signal $\Delta t^{+}_{\text{peak}}$ (Insert in Fig. 12).

The most striking result emerges in stronger convection ($\zeta \geq$ 4.23). Dual peaks are observed at ζ = 4.23, distinguishing it markedly from the weaker convection ($\zeta \leq$ 2.03). Comparing the cases at ζ = 2.03 and ζ =4.23 (moderate convection), substantial differences manifest in the following parameters: $\Delta t^{+}_{\text{max}}$, $R_{w_L,uw_S}(\Delta t^{+}_{\text{max}})$, and the streamwise integral lengthscales $L_{uu,x}$ and $L_{ww,x}$ [52]. The latter is particularly indicative of the disappearing convective rolls at ζ = 4.23. These disparities suggest that distinct mechanisms govern the peaks at their respective $\Delta t^{+}_{\text{max}}$. Stronger convection leads to more pronounced changes ($\zeta \geq$ 6.93). Notably, $R_{w_L,uw_S}(\Delta t^{-}_{\text{max}})$ surges rapidly with increasing ζ. Its sign is consistent with that of $R_{w_L,uw_S}(\Delta t = 0)$ so buoyancy dominates thermal plume development. Therefore, the primary distinction between strong convection and shear-dominant conditions lies in the phase difference between the signals. In such states, w_L is characterized by large-scale plumes that precede the small scales $E'_L(uw_S)$.

Our analysis demonstrates that ABL stability tightly influences the phase difference in the AM within UCL. A pivotal observation is the

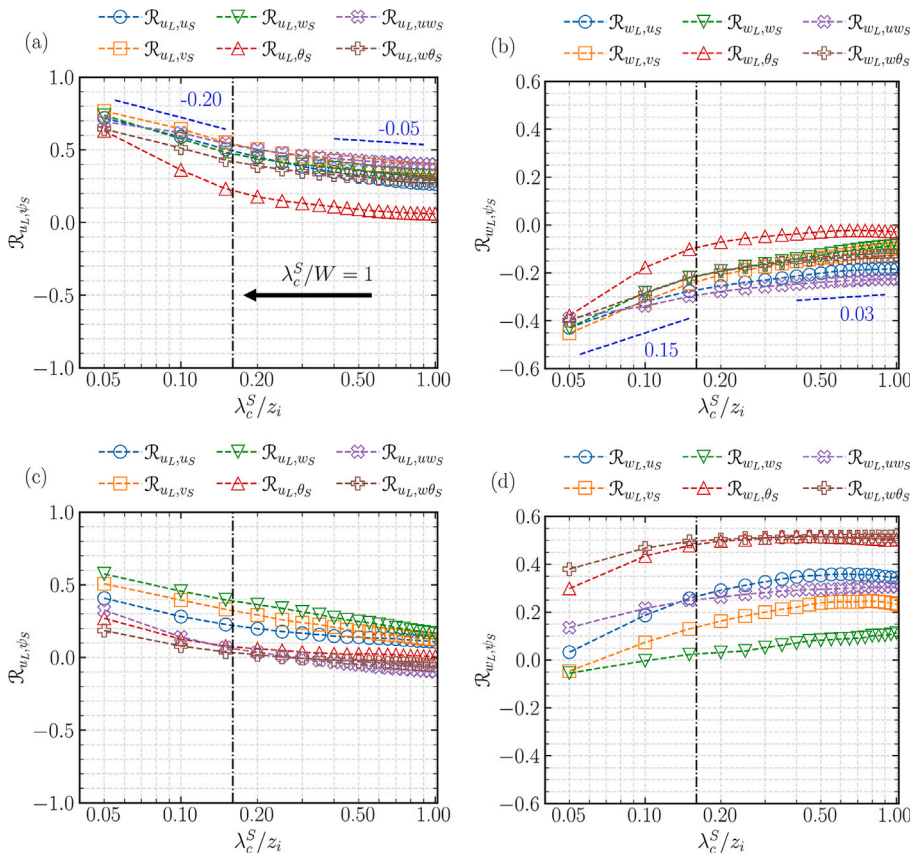

Fig. 11. Integrated AM coefficients $\mathcal{R}_{\varphi_L,\psi_S}$ at point P2 plotted against the small-scale cutoff wavelength λ_c^S in weak (ζ = 0.57; (a) and (b)) and strong (ζ = 48.31; (c) and (d)) convection. (a) and (c): $\mathcal{R}_{u_L,\psi_S}$; (b) and (d): $\mathcal{R}_{w_L,\psi_S}$. The blue dashed lines and texts in (a) and (b) approximate the slope scaling k_s by assuming $\mathcal{R}_{\varphi_L,\psi_S} \sim k_s \ln(\lambda_c^S)$.

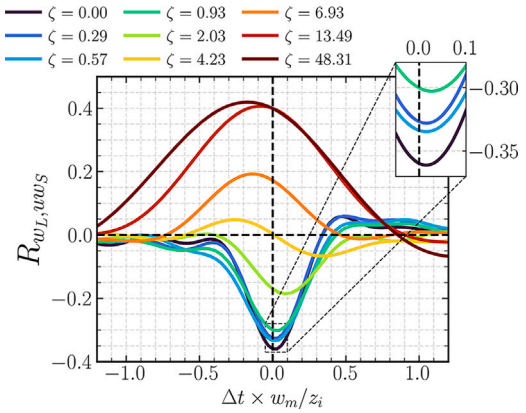

Fig. 12. Amplitude modulation coefficients R_{w_L,uw_S} ($z/H = 0.75, \Delta t$) plotted as functions of dimensionless time lag $\Delta t \times w_m/z_i$ under different stability ζ. The horizontal and vertical dashed lines represent zero-discriminant lines. The insert enlarges R_{w_L,uw_S} in neutral and weak convection.

alteration in the sequence of leading signals over time. While a comprehensive investigation into the underlying physics of this reversal is beyond the scope of this study, we hypothesize that this shift could be associated with a transition in small-scale turbulence generation, evolving from a "top-down" (convective rolls) to a "bottom-up" (thermal plumes) influence.

From a practical perspective, the impact of strong convection complicates the application of predictive models to urban CBLs. It is vital to preserve phase information during the calibration of two-point, data-driven predictive models, which are typically designed for neutral UBLs [38]. This requirement is even more critical in strong convection. In such settings, the presence of thermal plumes requires more stringent calibration criteria, including extended time intervals, to adequately capture the AM. Recent advancements in resolvent analysis offer promising analytical tools for predicting the phase difference between large-scale structures and near-wall momentum fluxes [70], as well as the roll-type coherence in shear-dominant CBLs [21]. Nevertheless, the augmented non-linearity stemming from stronger convection substantially alters UCL AM. Thus, it necessitates a cautious approach and an extensive development for the application of analytical predictive models, especially the strong convection ones, in urban CBLs,

5. Conclusion

In contemporary urban climatology research, comprehending the interactions between ABL-scale coherent structures and urban-scale turbulence is crucial. This study explores these multi-scale interactions within urban CBLs using the single-point AM approach [18]. The time-series dataset is the LESs conducted over an array of idealized urban morphology. The ABL stability ranges from neutral (ζ = 0.00) to near-free convective (ζ = 48.31) to contrast the dynamics attributed to streamwise rolls and thermal plumes. The LESs calculate the flows around explicitly resolved urban roughness elements to initiate small-scale UCL turbulence in response to wind-building interaction. The key findings of this study are depicted in a conceptual manner (Fig. 13) that are delineated as follows:

- In canopy regions, large-scale accelerating flows incite intense, small-scale turbulence intensities and fluxes, as indicated by the positive R_{u_L,ψ_S}. While the ABL is transitioning from neutral to

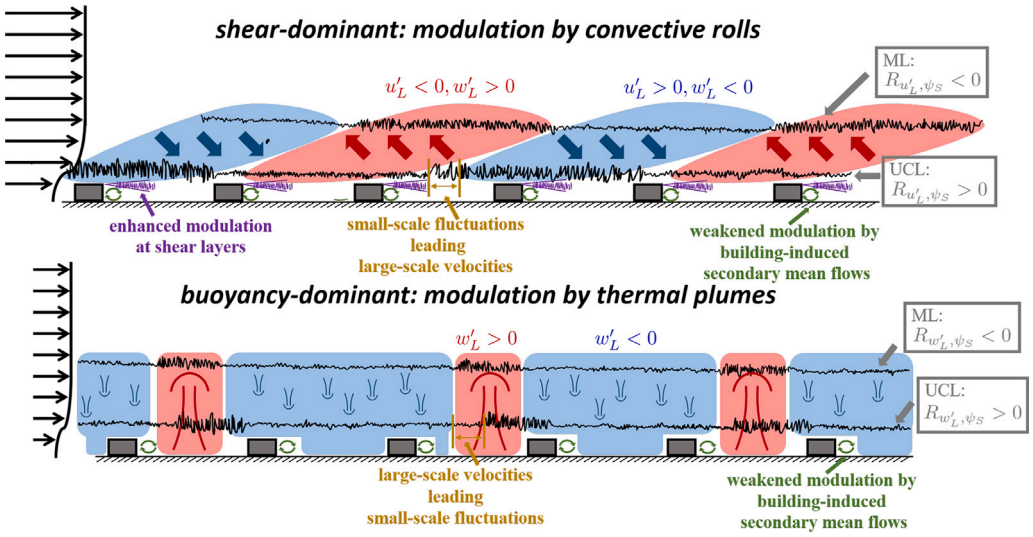

Fig. 13. Conceptual schematic of the amplitude modulation (AM) phenomena in urban convective boundary layers (CBLs). Thin black lines denote the signals of small-scale turbulent processes. The mixed layer and urban canopy layer are abbreviated to ML and UCL respectively. UCL signals are plotted over the rooftops for clarity.

strong convective, there exists a monotonic decrease in AM of small-scale turbulence by large-scale streamwise velocity u_L. This trend is attributed to the increased buoyancy and weakened streamwise coherence in large-scale CBL structures.

- In urban CBLs, the AM of small scales by large-scale vertical velocity w_L is more pronounced in the UCLs. This manifests differently under varying stabilities: large-scale downdrafts intensify small-scale turbulence in shear-dominant CBLs. Whilst, updrafts amplify them in buoyancy-dominant conditions. This phenomenon is a consequence of the transition of coherent structures from convective rolls to thermal plumes when the CBL is evolving toward stronger convection.
- We observe a non-monotonic trend in the AM of small scales by large-scale streamwise velocities in the mixed layers of CBLs in stronger convection. This observation implies that the organization and coherence of convective rolls would play key roles, influencing the AM of small scales therein.
- Other than large-scale CBL structures, building-induced flows, such as the primary recirculation in building wakes, dominate the AM of small-scale turbulence adjacent to buildings. In shear-dominant flows, the most pronounced AM from large-scale accelerations is found in the shear layers downstream buildings.
- The susceptibility of building-scale turbulence ($\lambda_x < W$) to the AM by large-scale (streamwise) flows is evident in both weak ($\zeta = 0.57$) and strong ($\zeta = 48.31$) convection. A steeper scaling slope k_s of AM coefficients observed at bulding-scale wavelengths indicates a more pronounced multi-scale interaction between CBL structures and roughness elements.
- Unstable stability profoundly modifies the phase relationship between large-scale vertical velocity w_L and small-scale turbulence within UCLs. Specifically, in strong convection, which is characterized by pronounced large-scale updrafts within thermal plumes, a leading phase relationship of w_L is observed with respect to the small-scale turbulence. This scenario contrasts markedly with that observed in neutral and weak convection.

In summary, this study systematically investigates the AM in urban CBLs based upon prior research that primarily focused on isothermal UBLs [34,36,37] and canonical CBLs [26]. Beyond aligning with previous findings, this study enriches the understanding of urban climate by elucidating the influence of large-scale structures on UCL dynamics.

The findings of this study also have significant practical implications. Recent advancements in the prediction of mean-wind-speed profiles in canonical settings, achieved by incorporating the effects of CBL coherent structures into the framework of the MOST, demonstrating this potential [10]. Despite these advancements, the influence of energetic CBL structures – which could induce spatiotemporal variability of UCL turbulence and fluxes as reported here – remains underrepresented in the land-surface parameterization of NWP models. Future research could be benefited from addressing the multi-scale AM within UCL models.

Furthermore, enhancing the performance of online NWP models presents a promising avenue, particularly through the application of predictive models that utilize outer-layer flow information to estimate UCL momentum and heat fluxes. Our results highlight several critical factors that should not be overlooked in model development and application. These include the impacts of building-induced mean flows, especially from high-rise structures, which can potentially undermine model accuracy. Besides, the degree of ABL stability warrants consideration in the implementation of predictive models because of the multi-scale interaction of AM and phase relationship.

Future research should be formulated upon the multi-scale analysis of turbulent flows, particularly through AM analysis, by transitioning to real-world scenarios. One critical area involves evolving from idealized, uniformly distributed to realistic, heterogeneously distributed surface heating. Given surface thermal heterogeneities significantly influence mean flows and transport processes in CBLs [50,71]. The effect of such heterogeneities on AM has yet to be investigated. Additionally, realistic urban morphologies, which are characterized by inhomogeneously distributed buildings of multi-scale geometries and complexity [36,72,73], profoundly impact the dynamics of turbulent flows within and above urban canopies. This influence subsequently alter large-scale, CBL modulation processes. Furthermore, the role of AM in stably stratified UBLs, which are commonly observed over urban areas during nighttime [74], presents a promising research direction. In stable atmospheric boundary layers (SABLs), flow structures, such as low-level jets (LLJs) and internal gravity waves, are prevalent [75]. Although recent studies suggested a major reduction in AM within canonical SABLs [76], the potential modulation of building-scale turbulence by large-scale flows in stable conditions, alike their unstable counterparts, needs further exploration. Thus, an in-depth understanding of these multi-scale interactions remains a valuable, crucial frontier in turbulence research and atmospheric sciences.

CRediT authorship contribution statement

Kangcheng Zhou: Writing – original draft, Visualization, Software, Methodology, Investigation, Formal analysis, Data curation. **Chun-Ho**

Liu: Writing – review & editing, Supervision, Project administration, Conceptualization. **Di Mei:** Writing – original draft, Data curation. **Buchen Wu:** Writing – review & editing, Visualization, Methodology, Data curation. **Minping Wan:** Writing – review & editing, Supervision, Resources, Project administration, Funding acquisition, Conceptualization.

Declaration of competing interest

The authors declare that they have no known competing financial interests or personal relationships that could have appeared to influence the work reported in this paper.

Data availability

Data will be made available on request.

Acknowledgments

This work was supported by the National Natural Science Foundation of China (Grant No. 12225204), the Shenzhen Science and Technology Program, China (Grant No. KQTD20180411143441009) and the Department of Science and Technology of Guangdong Province, China (Grant Nos. 2023B1212060001 and 2020B1212030001). Numerical simulations have been supported by the Center for Computational Science and Engineering of Southern University of Science and Technology, China.

References

[1] World Bank, World urbanization prospects: 2018 revision, 2018.
[2] Akexandra Witze, The deadly impact of urban heat, Nature 595 (2021) 349.
[3] Matthew A Nelson, Patrick Conry, Keeley R Costigan, Michael J Brown, Scott Meech, Dragan Zajic, Paul E Bieringer, Andrew Annunzio, George Bieberbach, A case study of the weather research and forecasting model applied to the joint urban 2003 tracer field experiment. Part III: Boundary-layer parametrizations, Bound.-Layer Meteorol. 183 (3) (2022) 381–405.
[4] Young-Hee Ryu, Jong-Jin Baik, Sang-Hyun Lee, A new single-layer urban canopy model for use in mesoscale atmospheric models, J. Appl. Meteorol. Climatol. 50 (9) (2011) 1773–1794.
[5] Ingegärd Eliasson, Brian Offerle, CSB Grimmond, Sven Lindqvist, Wind fields and turbulence statistics in an urban street canyon, Atmos. Environ. 40 (1) (2006) 1–16.
[6] AA Aliabadi, M Moradi, D Clement, WD Lubitz, B Gharabaghi, Flow and temperature dynamics in an urban canyon under a comprehensive set of wind directions, wind speeds, and thermal stability conditions, Environ. Fluid Mech. 19 (2019) 81–109.
[7] Amir A. Aliabadi, Mohsen Moradi, Ryan A.E. Byerlay, The budgets of turbulence kinetic energy and heat in the urban roughness sublayer, Environ. Fluid Mech. 21 (4) (2021) 843–884.
[8] Hiroyuki Kusaka, Fujio Kimura, Coupling a single-layer urban canopy model with a simple atmospheric model: Impact on urban heat island simulation for an idealized case, J. Meteorol. Soc. Jpn. Ser. II 82 (1) (2004) 67–80.
[9] Alberto Martilli, Alain Clappier, Mathias W. Rotach, An urban surface exchange parameterisation for mesoscale models, Bound.-Layer Meteorol. 104 (2002) 261–304.
[10] S.T. Salesky, W. Anderson, Coherent structures modulate atmospheric surface layer flux-gradient relationships, Phys. Rev. Lett. 125 (12) (2020) 124501.
[11] Nicholas Hutchins, Ivan Marusic, Large-scale influences in near-wall turbulence, Phil. Trans. R. Soc. A 365 (1852) (2007) 647–664.
[12] I. Marusic, R. Mathis, N. Hutchins, Predictive model for wall-bounded turbulent flow, Science 329 (5988) (2010) 193–196.
[13] Kyung Chun Kim, Ronald J. Adrian, Very large-scale motion in the outer layer, Phys. Fluids 11 (2) (1999) 417–422.
[14] Jae Hwa Lee, Hyung Jin Sung, Very-large-scale motions in a turbulent boundary layer, J. Fluid Mech. 673 (2011) 80–120.
[15] Ulf Högström, J.C.R. Hunt, Ann-Sofi Smedman, Theory and measurements for turbulence spectra and variances in the atmospheric neutral surface layer, Bound.-Layer Meteorol. 103 (2002) 101–124.
[16] B.J. Balakumar, R.J. Adrian, Large-and very-large-scale motions in channel and boundary-layer flows, Phil. Trans. R. Soc. A 365 (1852) (2007) 665–681.
[17] Sergio Hoyas, Javier Jiménez, Scaling of the velocity fluctuations in turbulent channels up to Re_τ=2003, Phys. Fluids 18 (1) (2006).
[18] Romain Mathis, Nicholas Hutchins, Ivan Marusic, Large-scale amplitude modulation of the small-scale structures in turbulent boundary layers, J. Fluid Mech. 628 (2009) 311–337.
[19] Samir Khanna, James G. Brasseur, Three-dimensional buoyancy-and shear-induced local structure of the atmospheric boundary layer, J. Atmos. Sci. 55 (5) (1998) 710–743.
[20] Balaji Jayaraman, James G. Brasseur, Transition in atmospheric boundary layer turbulence structure from neutral to convective, and large-scale rolls, J. Fluid Mech. 913 (2021) A42.
[21] Gabriel YR Hamada, William R Wolf, Diogo B Pitz, Leonardo S de B Alves, Stability and receptivity analyses of mixed convection in unstably stratified horizontal boundary layers, J. Fluid Mech. 961 (2023) A10.
[22] Carlo Cossu, Onset of large-scale convection in wall-bounded turbulent shear flows, J. Fluid Mech. 945 (2022) A33.
[23] Qi Li, Pierre Gentine, Juan Pedro Mellado, Kaighin A McColl, Implications of nonlocal transport and conditionally averaged statistics on Monin–Obukhov similarity theory and townsend's attached eddy hypothesis, J. Atmos. Sci. 75 (10) (2018) 3403–3431.
[24] S.T. Salesky, W. Anderson, Buoyancy effects on large-scale motions in convective atmospheric boundary layers: implications for modulation of near-wall processes, J. Fluid Mech. 856 (2018) 135–168.
[25] Laurent Perret, Edward G. Patton, Stability influences on interscale transport of turbulent kinetic energy and Reynolds shear stress in atmospheric boundary layers interacting with a tall vegetation canopy, J. Fluid Mech. 921 (2021) A14.
[26] Scott T. Salesky, Marcelo Chamecki, Elie Bou-Zeid, On the nature of the transition between roll and cellular organization in the convective boundary layer, Bound.-Layer Meteorol. 163 (2017) 41–68.
[27] Jian-Zhao Wu, Bo-Fu Wang, Quan Zhou, Massive heat transfer enhancement of Rayleigh–Bénard turbulence over rough surfaces and under horizontal vibration, Acta Mech. Sin. 38 (2) (2022) 321319.
[28] Seung-Bu Park, Jong-Jin Baik, Large-eddy simulations of convective boundary layers over flat and urbanlike surfaces, J. Atmos. Sci. 71 (5) (2014) 1880–1892.
[29] K.M. Talluru, R. Baidya, N. Hutchins, Ivan Marusic, Amplitude modulation of all three velocity components in turbulent boundary layers, J. Fluid Mech. 746 (2014) R1.
[30] Romain Mathis, Ivan Marusic, Nicholas Hutchins, KR Sreenivasan, The relationship between the velocity skewness and the amplitude modulation of the small scale by the large scale in turbulent boundary layers, Phys. Fluids 23 (12) (2011).
[31] Subrahmanyam Duvvuri, Beverley J. McKeon, Triadic scale interactions in a turbulent boundary layer, J. Fluid Mech. 767 (2015) R4.
[32] M. Inoue, Romain Mathis, Is Marusic, D.I. Pullin, Inner-layer intensities for the flat-plate turbulent boundary layer combining a predictive wall-model with large-eddy simulations, Phys. Fluids 24 (7) (2012).
[33] Muhammad Nadeem, Jae Hwa Lee, Jin Lee, Hyung Jin Sung, Turbulent boundary layers over sparsely-spaced rod-roughened walls, Int. J. Heat Fluid Flow 56 (2015) 16–27.
[34] William Anderson, Amplitude modulation of streamwise velocity fluctuations in the roughness sublayer: evidence from large-eddy simulations, J. Fluid Mech. 789 (2016) 567–588.
[35] Jérémy Basley, Laurent Perret, Romain Mathis, Spatial modulations of kinetic energy in the roughness sublayer, J. Fluid Mech. 850 (2018) 584–610.
[36] Yixun Liu, Chun-Ho Liu, Guy P Brasseur, Christopher YH Chao, Amplitude modulation of velocity fluctuations in the atmospheric flows over real urban morphology, Phys. Fluids 35 (2) (2023).
[37] Ruiqi Wang, Chun-Ho Liu, Fei Li, Ziwei Mo, Turbulent transport mechanism in the roughness sublayers over idealized urban areas and its implication to street-level ventilation, Sustainable Cities Soc. 100 (2024) 105030.
[38] Karin Blackman, Laurent Perret, Romain Mathis, Assessment of inner–outer interactions in the urban boundary layer using a predictive model, J. Fluid Mech. 875 (2019) 44–70.
[39] Margaret A. Lemone, Modulation of turbulence energy by longitudinal rolls in an unstable planetary boundary layer, J. Atmos. Sci. 33 (7) (1976) 1308–1320.
[40] Eslam R Lotfy, Ashraf A Abbas, Sheikh Ahmad Zaki, Zambri Harun, Characteristics of turbulent coherent structures in atmospheric flow under different shear–buoyancy conditions, Bound.-Layer Meteorol. 173 (2019) 115–141.
[41] W.C. Cheng, Chun-Ho Liu, Large-eddy simulation of turbulent transports in urban street canyons in different thermal stabilities, J. Wind Eng. Ind. Aerodyn. 99 (4) (2011) 434–442.
[42] G. Duan, K. Ngan, Sensitivity of turbulent flow around a 3-D building array to urban boundary-layer stability, J. Wind Eng. Ind. Aerodyn. 193 (2019) 103958.
[43] Huatao Ma, Wai-Chi Cheng, Effects of unstable thermal stratification on the flow characteristics in an idealized rural-to-urban transition region: A large-eddy simulation study, Build. Environ. 230 (2023) 109971.
[44] Junjie Cai, Jingtan Chen, Haimei Cheng, Shuangfei Zi, Jinchao Xiao, Fan Xia, Jiyun Zhao, The effects of thermal stratification on airborne transport within the urban roughness sublayer, Int. J. Heat Mass Transfer 184 (2022) 122289.
[45] Chin-Hoh Moeng, A large-eddy-simulation model for the study of planetary boundary-layer turbulence, J. Atmos. Sci. 41 (13) (1984) 2052–2062.
[46] James W. Deardorff, Stratocumulus-capped mixed layers derived from a three-dimensional model, Bound.-Layer Meteorol. 18 (4) (1980) 495–527.

[47] Matt Churchfield, Sang Lee, NWTC design codes (SOWFA), 2013, http://wind.nrel.gov/designcodes/simulators/SOWFA.
[48] Zhengtong Xie, Ian P. Castro, LES and RANS for turbulent flow over arrays of wall-mounted obstacles, Flow Turbul. Combust. 76 (3) (2006) 291–312.
[49] W.C. Cheng, Chun-Ho Liu, Large-eddy simulation of flow and pollutant transports in and above two-dimensional idealized street canyons, Bound.-Layer Meteorol. 139 (2011) 411–437.
[50] Fabien Margairaz, Eric R. Pardyjak, Marc Calaf, Surface thermal heterogeneities and the atmospheric boundary layer: the relevance of dispersive fluxes, Bound.-Layer Meteorol. 175 (2020) 369–395.
[51] John C. Wyngaard, Turbulence in the Atmosphere, Cambridge University Press, 2010.
[52] Kangcheng Zhou, Chun-Ho Liu, Minping Wan, Large-scale coherent structure and canopy-level turbulence in the convective boundary layer over urban areas, Build. Environ. 244 (2023) 110733.
[53] Diana M. Cancelli, Marcelo Chamecki, Nelson L. Dias, A large-eddy simulation study of scalar dissimilarity in the convective atmospheric boundary layer, J. Atmos. Sci. 71 (1) (2014) 3–15.
[54] Edward G Patton, Peter P Sullivan, Roger H Shaw, John J Finnigan, Jeffrey C Weil, Atmospheric stability influences on coupled boundary layer and canopy turbulence, J. Atmos. Sci. 73 (4) (2016) 1621–1647.
[55] Ian P. Castro, Hong Cheng, Ryan Reynolds, Turbulence over urban-type roughness: deductions from wind-tunnel measurements, Bound.-Layer Meteorol. 118 (2006) 109–131.
[56] Haiping Tian, Xingrui Yi, Fang Xu, Fen Li, Nan Jiang, Lagrangian-based spatial-temporal topological study on the evolution and migration of coherent structures in wall turbulence, Acta Mech. Sin. 38 (1) (2022) 321465.
[57] K. Nozawa, T. Tamura, Large eddy simulation of the flow around a low-rise building immersed in a rough-wall turbulent boundary layer, J. Wind Eng. Ind. Aerodyn. 90 (10) (2002) 1151–1162.
[58] K.R. Sreenivasan, On the fine-scale intermittency of turbulence, J. Fluid Mech. 151 (1985) 81–103.
[59] John M Edwards, Anton CM Beljaars, Albert AM Holtslag, Adrian P Lock, Representation of boundary-layer processes in numerical weather prediction and climate models, Bound.-Layer Meteorol. 177 (2–3) (2020) 511–539.
[60] Karin Blackman, Laurent Perret, Non-linear interactions in a boundary layer developing over an array of cubes using stochastic estimation, Phys. Fluids 28 (9) (2016).
[61] Woutijn J Baars, KM Talluru, Nicholas Hutchins, Ivan Marusic, Wavelet analysis of wall turbulence to study large-scale modulation of small scales, Exp. Fluids 56 (2015) 1–15.
[62] Yixun Liu, Chun-Ho Liu, Guy P Brasseur, Christopher YH Chao, Wavelet analysis of the atmospheric flows over real urban morphology, Sci. Total Environ. 859 (2023) 160209.
[63] Timothy R Oke, Gerald Mills, Andreas Christen, James A Voogt, Urban Climates, Cambridge University Press, 2017.
[64] Ankit Awasthi, William Anderson, Numerical study of turbulent channel flow perturbed by spanwise topographic heterogeneity: amplitude and frequency modulation within low-and high-momentum pathways, Phys. Rev. Fluids 3 (4) (2018) 044602.
[65] Chao Yuan, Ruiqin Shan, Yangyang Zhang, Xian-Xiang Li, Tiangang Yin, Jian Hang, Leslie Norford, Multilayer urban canopy modelling and mapping for traffic pollutant dispersion at high density urban areas, Sci. Total Environ. 647 (2019) 255–267.
[66] T. Okaze, A. Ono, A. Mochida, Y. Kannuki, S. Watanabe, Evaluation of turbulent length scale within urban canopy layer based on LES data, J. Wind Eng. Ind. Aerodyn. 144 (2015) 79–83.
[67] Hyeyum Hailey Shin, Domingo Muñoz-Esparza, Jeremy A Sauer, Matthias Steiner, Large-eddy simulations of stability-varying atmospheric boundary layer flow over isolated buildings, J. Atmos. Sci. 78 (5) (2021) 1487–1501.
[68] Sylvain Dupont, Edward G. Patton, On the influence of large-scale atmospheric motions on near-surface turbulence: Comparison between flows over low-roughness and tall vegetation canopies, Bound.-Layer Meteorol. 184 (2) (2022) 195–230.
[69] Hongyou Liu, Guohua Wang, Xiaojing Zheng, Amplitude modulation between multi-scale turbulent motions in high-Reynolds-number atmospheric surface layers, J. Fluid Mech. 861 (2019) 585–607.
[70] G. Cui, I. Jacobi, Prediction of the phase difference between large-scale velocity and Reynolds stress fluctuations in wall turbulence, J. Fluid Mech. 969 (2023) A13.
[71] Scott T. Salesky, M. Calaf, W. Anderson, Unstable turbulent channel flow response to spanwise-heterogeneous heat fluxes: Prandtl's secondary flow of the third kind, J. Fluid Mech. 934 (2022) A46.
[72] Takfarinas Medjnoun, Eduardo Rodriguez-Lopez, MA Ferreira, Tom Griffiths, Johan Meyers, Bharathram Ganapathisubramani, Turbulent boundary-layer flow over regular multiscale roughness, J. Fluid Mech. 917 (2021) A1.
[73] Michał Korycki, Lech Łobocki, Andrzej Wyszogrodzki, Numerical simulation of stratified flow around a tall building of a complex shape, Environ. Fluid Mech. 16 (2016) 1143–1171.
[74] Fenjuan Wang, Scott D Chambers, Zhenyi Zhang, Alastair G Williams, Xiaodong Deng, Hua Zhang, Giovanni Lonati, Jagoda Crawford, Alan D Griffiths, Antonietta Ianniello, et al., Quantifying stability influences on air pollution in Lanzhou, China, using a radon-based "stability monitor": Seasonality and extreme events, Atmos. Environ. 145 (2016) 376–391.
[75] Larry Mahrt, Stably stratified atmospheric boundary layers, Annu. Rev. Fluid Mech. 46 (2014) 23–45.
[76] Brian Greene, Stable Atmospheric Boundary Layer Turbulence: Insights from Uncrewed Aircraft System Observations and Large-Eddy Simulations (Ph.D. thesis), University of Oklahoma, 2022.